MusE GAs FLOw and Wind (MEGAFLOW) XII. Rationale and design of a Mg ii survey of the cool circum-galactic medium with MUSE and UVES: The MEGAFLOW Survey

Nicolas F Bouché, Martin Wendt, Johannes Zabl, Maxime Cherrey, Ilane Schroetter, Ivanna Langan, Sowgat Muzahid, Joop Schaye, Benoît Epinat, Lutz Wisotzki, et al.

Astronomy & Astrophysics manuscript no. megaflow_survey
November 12, 2024

MusE GAs FLOw and Wind (MEGAFLOW) XII. Rationale and design of a Mg II survey of the cool circum-galactic medium with MUSE and UVES: The MEGAFLOW Survey

Nicolas F. Bouché[1], Martin Wendt[2], Johannes Zabl[1,3], Maxime Cherrey[1], Ilane Schroetter[4], Ivanna Langan[1,5], Sowgat Muzahid[6], Joop Schaye[7], Benoît Epinat[8,9], Lutz Wisotzki[10], Thierry Contini[4], Johan Richard[1], Roland Bacon[1], and Peter M. Weilbacher[10]

(Affiliations can be found after the references)

Accepted October 24, 2024. Received June 12, 2024; in original form November 12, 2024

ABSTRACT

We present the design, rationale, properties and catalogs of the MusE Gas FLOw and Wind survey (MEGAFLOW), a survey of the cool gaseous halos of $z \simeq 1.0$ galaxies using low-ionization Mg II absorption systems. The survey consists of 22 quasar fields selected from the Sloan Digital Sky Survey (SDSS) having multiple (≥ 3) strong Mg II absorption lines over the redshift range $0.3 < z < 1.5$. Each quasar was observed with the Multi-Unit Spectroscopic Explorer (MUSE) and the Ultraviolet and Visual Echelle Spectrograph (UVES), for a total of 85 hr and 63 hr, respectively. The UVES data resulted in 127 Mg II absorption lines over $0.25 < z < 1.6$, with a median rest-frame equivalent width (REW) 3σ limit of ≈ 0.05 Å. The MUSE data resulted in $\sim$2400 galaxies of which 1403 with redshift confidence `ZCONF`> 1, i.e. more than 60 galaxies per arcmin^2. They were identified using a dual detection algorithm based on both continuum and emission line objects. The achieved [O II] 50% completeness is $3.7^{+0.8}_{-0.6} \times 10^{-18}$erg s^{-1} cm^{-2} (corresponding to SFR> 0.01 M$_\odot$ yr^{-1} at $z = 1$) using realistic mock [O II] emitters and the 50% completeness is $m_{F775W} \approx 26$ AB magnitudes for continuum sources. We find that (i) the fraction of [O II] emitting galaxies which have no continuum is $\sim 15\%$; (ii) the success rate in identifying at least one galaxy within 500 km s^{-1} and 100 kpc is $\approx 90\%$ for Mg II absorptions with $W_r^{2796} \gtrsim 0.5$ Å ; (iii) the mean number of galaxies per Mg II absorption is 2.9 ± 1.6 within the MUSE field-of-view; (iv) of the 80 Mg II systems at $0.3 < z < 1.5$, 40 (20) have 1 (2) galaxies within 100 kpc, respectively; (v) all but two host galaxies have stellar masses $M_\star > 10^9$ M$_\odot$, and star-formation rates > 1 M$_\odot$ yr^{-1}.

Key words. Galaxies: intergalactic medium; quasars: absorption lines; Galaxies: halos; Galaxies: evolution

1. Introduction

The circum-galactic medium (CGM) is the complex interface between the inter galactic medium and the galaxies themselves. Traditionally, the CGM describes the gas surrounding galaxies outside their disks or interstellar medium and inside their virial radii (Tumlinson et al. 2017). The CGM is the interface between the continuous fresh source of fuel coming from the IGM and star-formation driven outflows, often referred to as the baryon cycle (Péroux & Howk 2020). As a result, the CGM ought to retain the kinematical (and/or enrichment) signatures of these processes.

A significant amount of effort has been devoted to the study of galaxies close to QSO sight-lines to study the interplay between outflows and accretion. The idea of such a medium goes back to the detection of cold gas clouds toward stars at high Galactic latitudes (Spitzer 1956). Soon after the discovery of the first quasars, Bahcall & Spitzer (1969) proposed that most of the absorption lines observed in QSO spectra were caused by gas in extended halos of normal galaxies.

The most commonly used metal absorption in quasar spectra is the magnesium (Mg II) $\lambda\lambda 2796, 2803$ doublet, which is known to trace 'cool' ($T \sim 10^4$ K) photo-ionized gas in and around galaxies since Bergeron & Boissé (1991); Bergeron et al. (1992, 1994); Steidel (1993) and Steidel et al. (1994). In the vicinity of galaxies, Mg II absorptions are expected to occur in sightlines probing either outflows (as in Nestor et al. 2011) or accreting gas in extended gaseous disks (Fumagalli et al. 2011; Pichon et al. 2011; Kimm et al. 2011; Shen et al. 2013; DeFelippis et al. 2021). Strong Mg II absorptions, with REW $W_r^{2796} > 1$ Å can also occur in groups (e.g. Kacprzak et al. 2010; Gauthier 2013; Bielby et al. 2017) and weak Mg II absorptions ($W_r^{2796} < 0.1$ Å) in the outskirts of clusters (e.g. Mishra & Muzahid 2022).

Thanks to the Sloan Digital Sky Survey (SDSS, York et al. 2000), the detection of tens of thousands of Mg II absorbers with $W_r^{2796} \gtrsim 0.5$ Å (e.g. Nestor et al. 2005; Zhu & Ménard 2013) have enabled statistical analyses (e.g. Bouché et al. 2006; Lundgren et al. 2009; Gauthier et al. 2009). As noted in Nestor et al. (2005) and subsequently , the REW W_r^{2796} distribution is a double exponential, where the transition occurs at around $W_r^{2796} \simeq 0.5$ Å indicating a transition between strong and weak Mg II systems possibly related to different physical mechanisms. This is supported by the different redshift evolution of strong and weak Mg II systems (Nestor et al. 2005).

But, connecting the kinematics of the gas in/ouflow processes to the kinematics of the host galaxy requires one to be able to identify the host efficiently. The advent of the Multi Unit Spectroscopic Explorer (MUSE Bacon et al. 2010) on the Very Large Telescope (VLT) has revolutionised the study of the CGM thanks to its exquisite sensitivity and

its field of view (FOV). As a result, a number of MUSE-based CGM surveys have been developed over the past few years such as QSAGE (Bielby et al. 2019), MUSEQuBES (Muzahid et al. 2020), CUBES (Chen et al. 2020), MAGG Lofthouse et al. (2020), and MUSE-ALMA (Péroux et al. 2019).

This paper describes the rationale, design and properties of the MusE GAs FLOw and Wind (MEGAFLOW) survey, a Mg II-selected survey around 22 QSO fields. This paper is part of a series of 12 papers (Schroetter et al. 2016, 2019, 2021, 2024; Zabl et al. 2019, 2020, 2021; Wendt et al. 2021; Freundlich et al. 2021; Langan et al. 2023; Cherrey et al. 2024, 2025) and is organized as follows. In section § 2, we present the survey design and rationale. For each of the 22 quasar fields, we have MUSE observations (from 2 to 11hr) and obtained high-quality UVES spectra, as discussed in section 3. In § 4, we present the methods used to generate the catalogs of Mg II absorbers and galaxies. In § 5, we describe the physical properties of the galaxies. In § 6, we present the main properties of the host galaxies. In § 7, we compare our sample to others. Conclusions are described in § 8.

Throughout, we use a Λ cold dark matter (ΛCDM) model with $\Omega_M = 0.307$, $\Omega_\Lambda = 0.693$ and $H_0 = 67$ km s^{-1} Mpc^{-1} ('Planck 2015' Planck Collaboration et al. 2016). At the typical redshift of our survey $z = 1$, $1''$ corresponds to 8.23 kpc. All magnitudes are in the AB system.

2. MEGAFLOW survey design and rationale

The low-ionization Mg II$\lambda\lambda$2796, 2803 doublet seen in quasar spectra has been recognized as a good tracer of the cool ($T \sim 10^4$ K) CGM for about thirty years (e.g. Bergeron & Boissé 1991; Bergeron et al. 1992; Steidel et al. 1995, 1997, 2002). But, finding the galaxy counterpart associated to the Mg II absorption is often a complicated process which, before the advent of integral field spectrographs (IFS), required deep pre-imaging in order to identify host-galaxy candidates and expensive spectroscopic follow-up campaigns to secure the host galaxy identification from its redshift (e.g. Bergeron & Boissé 1991; Steidel et al. 1997; Chen & Tinker 2008; Chen et al. 2010b,a; Churchill et al. 2013; Nielsen et al. 2013a,b). However, the imaging+spectroscopy technique suffers from several disadvantages: (i) it is inefficient, requiring multiple campaigns, for imaging, for redshift identification and for kinematics determination (e.g. Kacprzak et al. 2011; Ho et al. 2019); (ii) it is biased against emission-line galaxies given that pre-imaging necessary for the pre-identification of host-galaxy candidates is based on the continuum light; and (iii) it is challenging close to the line-of-sight (LOS) due to the quasar point spread function (PSF).

These shortcomings can be bypassed using Integral Field Unit (IFU) spectroscopy such as SINFONI (Eisenhauer & et al. 2003) or the Multi-Unit-Spectrograph Explorer instrument (Bacon et al. 2010) given that it allows the identification of the galaxy counterpart without pre-imaging as demonstrated in Bouché et al. (2007). In addition, IFU observations also provide the host kinematics and the morphological information which are both easily determined from such 3D data. Furthermore, 3D data offers the possibility to easily subtract the quasar's PSF.

The exquisite sensitivity and large field-of-view ($1' \times 1'$) of MUSE allows one to detect galaxies further from the quasar ($30''$ or $\sim$250 kpc at $z = 1$) and its large wavelength coverage (4700Å to 9300Å) allows one to target quasar sight-lines with multiple Mg II $\lambda\lambda$2796, 2803 absorption lines over the redshift range from 0.4 to 1.5 suitable for the identification of [O II] emitting galaxies.

The MEGAFLOW survey aims at building a statistical sample with at least 100+ galaxy-quasar pairs (i.e. 10× larger than our SINFONI survey, Bouché et al. 2007) in order to allow for a robust analysis of the relation between the absorption and the host galaxy properties. To this end, we selected quasars with (i) at least three ($N_{\rm abs} \geq 3$) Mg II$\lambda\lambda$2796, 2803 absorption lines at redshifts between 0.4 and 1.4, — ensuring that a sample $\sim$ 100 galaxy-quasar pairs could be build with only 20-25 quasar LOS — and (ii) with a REW $W_{\rm r}^{2796} \gtrsim 0.5$Å from the Zhu & Ménard (2013) Mg II catalog of 100,000 Mg II absorption lines extracted from 400,000 quasar spectra in SDSS (DR12) [1]. The latter criteria ensures that the host galaxies are within 100 kpc from the quasar LOS (at $z \sim 1$), i.e. within the MUSE field-of-view, given the well known anti-correlation between the impact parameter and rest-frame equivalent width $W_{\rm r}^{2796}$ (Lanzetta & Bowen 1990; Steidel 1995).

In the end, the MEGAFLOW survey is made of 22 quasar fields listed in Table 1 and the above selection criteria resulted in a sample of 79 Mg II absorbers with $W_{\rm r}^{2796} \gtrsim 0.5$Å. This survey is thus optimized to study the properties of galaxies associated with strong Mg II absorption lines, but given the wide wavelength range, it also allows one to perform galaxy-centered analysis such as the covering fraction (Schroetter et al. 2021; Cherrey et al. 2024). We discuss further the impact of the MEGAFLOW selection criteria on such analysis in section § 6.6.

As part of the MEGAFLOW series, in Schroetter et al. (2016) and Schroetter et al. (2019), we presented a preliminary analysis on quasars probing galactic outflows. In Zabl et al. (2019), we presented a preliminary analysis on quasars probing extended gaseous disks, based on a first version of the galaxy catalog, referred to as 'DR1'. In Zabl et al. (2020), we presented a first tomographic study of an outflow probed by two background sources. In Zabl et al. (2021), we presented an extended Mg II map of the outflowing material around a $z = 0.7$ star-forming galaxy. In Wendt et al. (2021), we presented a first analysis of the metallicity/dust content of the CGM as a function of azimuthal angle. In Schroetter et al. (2021), we presented a first analysis on the Mg II and C IV covering fractions at $z > 1$. In Freundlich et al. (2021), we presented a first attempt at detecting the molecular gas content of a subset of galaxies. In Langan et al. (2023), we presented an analysis of the impact of gas in/outflows on the main-sequence and mass-metallicity scaling relations. In Cherrey et al. (2024), we presented an analysis of the Mg II covering fractions in groups of galaxies. In Cherrey et al. (2025), we presented an analysis of the Mg II covering fration of isolated galaxies.

[1] Available at `https://www.guangtunbenzhu.com/jhu-sdss-metal-absorber-catalog`.

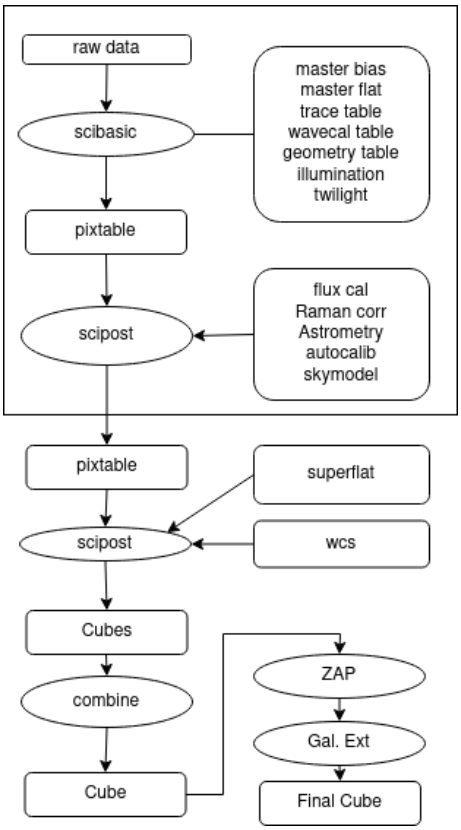

Fig. 1: Schematic diagram of the steps in the data reduction process.

3. Data

In section 3.1, we describe the MUSE data and data reduction and in section 3.2, we describe the UVES data reduction.

3.1. MUSE data

The MUSE observations were conducted in visitor mode between 2014 and 2018 using guarantee time observations (GTO). The data were acquired in Wide Field Mode (WFM), using both standard (WFM-NOAO-N) and adaptive-optics (WFM-AO-N) modes - the latter having been available since Fall 2017, following the commissioning of the ground layer Adaptive Optics (AO) facility. This implies that the AO observations have a gap at 5800–5980 Å due to the AO notch filter. As a result, some of the combined (AO+ non-AO) datasets have a very heterogeneous PSF in that spectral region. The program IDs, total exposure times and the final image quality are listed in Table 2.

In order to produce a fully calibrated 3D-cube, we used the standard recipes from the MUSE data reduction pipeline (version $\geq$2.4) (Weilbacher et al. 2014, 2020), and supplemented some post-processing with custom routines following Bacon et al. (2017), Zabl et al. (2019) and Bacon et al. (2023) with some differences. The sequence of steps is illustrated schematically in Fig. 1.

First, raw night calibration exposures are combined to produce a master bias, master flat and trace table (which locates the edges of the slitlets on the detectors). These calibrations are then applied to all the raw science exposures with the `scibasic` recipe. Bad pixels corresponding to known CCD defects (columns or pixels) are also masked to reject known detector defects. Furthermore, the `scibasic` recipe performs geometric and wavelength calibrations. At this point, the pipeline product is a pixel table (hereafter called *pixtable*) containing all pixel information: location, wavelength, photon count and an estimate of the variance.

While the flat-fielding with lamp flats done in the `scibasic` step removes pixel-to-pixel sensitivity variations, it is not sufficient to ensure an even illumination, especially across the different IFUs. Twilight exposures and night-time internal flat calibrations (called illumination corrections) are used, when available, for additional correction in order to correct for these flux variations at the slice edges which depends on the ambient temperature. We always use the illumination taken at a similar time and/or with an ambient temperature closer to that of the science exposures.

Next, the `scipost` recipe performs the atmospheric dispersion correction, barycentric velocity correction, astrometric calibration, telluric correction and flux calibration on the pixtable. Regarding the flux calibration, observations of spectro-photometric standard stars are reduced in the same way as the science data (save the flux-calibration). The spectral response function used for flux-calibration of the science data is determined by comparing the star's spectrum to tabulated reference fluxes.

As described in Bacon et al. (2023) (their Fig.B1), one can still see a low-level footprint of the instrumental slices and channels which arises from imperfect flat-fielding, which are difficult to correct for with standard calibration exposures as illustrated on Fig. 2a. The procedure (referred to as 'auto-calibration') to correct for this starts by masking all bright objects in the data using the white-light image as described in the Appendix B.2 of Bacon et al. (2023). The algorithm calculates the median background flux level in each slice (before sky-subtraction) using only the unmasked voxels and then scale all slices to the mean flux of all slices using a robust outliers rejection (15σ clipping of the median absolute deviation). This slice normalization is done in 20 wavelength bins of 200-300Å chosen so that their edges do not fall on a sky line. This self-calibration approach is implemented in the MUSE pipeline for versions $\geq$ 2.4 (see § 3.10.2 of Weilbacher et al. 2020).

Processing the data up to this point (box in Fig. 1) is standard and was performed with default parameters of the pipeline within the MuseWise framework [2] (Valentijn et al. 2017). Included at this stage are the removal of the sky telluric emission (OH lines and continuum) and of Raman lines induced by the lasers from the AO facility (Weilbacher et al. 2020, § 3.10.1).

One remaining imperfection even after the flat fielding steps and the per-slice auto-calibration are sharp flux drops at the edge of those slices which are located at edges of the IFUs. As discussed in Bacon et al. (2023) (their Appendix B.4), a way to improve upon these remaining imperfections is through the use of pseudo 'skyflats' (or superflats) generated from multiple exposures. This procedure requires to resample the *pixtable* into a cube sampled on the same instrumental grid turning off the dithering and rotations. This means that in order to create a skyflat for each exposure, one needs to resample all of the others (used as skyflat) to the grid of that exposure. With of the order 30 sky expo-

[2] `http://muse-dbview.target.rug.nl/`.

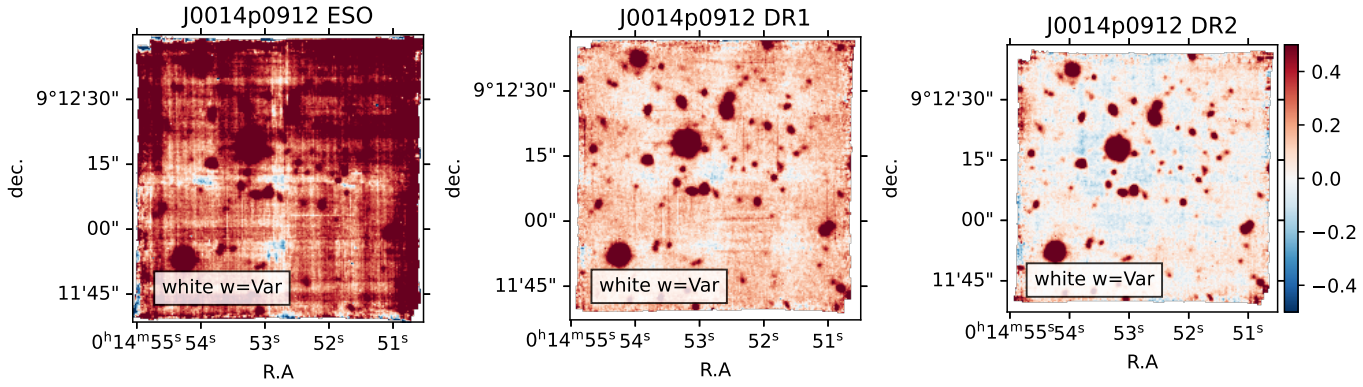

Fig. 2: White-light images (variance weighted) for the field J0014p0912 from different data-reductions. *Left*: Automatic data reduction from ESO. *Middle*: Data reduction ('DR1') using custom scripts as in Zabl et al. (2019). *Right*: Final data reduction ('DR2') used here using super flats (§ 3).

sures required to create a skyflat, the required amount of re-sampling is computationally very expensive.

In order to avoid this expensive computational effort, we created the pseudo skyflats from the `scipost` *pixtable* level, just before resampling the cubes. The pixtables produced by `scipost` contain fully flux calibrated - including all flat field steps described above, and we stacked these pixels. One practical necessity is to mask objects which are in the sky-exposures in the pixtables. An assumption here is that the flat-fielding imperfections, which we aim to catch with the sky-flat, are not shifting around on the detector.

Best suited exposures for constructing the sky-flats are observations of extragalactic deep fields, as they have a relatively sparse source density and hence substantial free sky. In order to have sufficient signal to form a skyflat, one needs 30-50 frames. In total, we constructed four sky-flats, for the GTO runs in Oct/Nov 2014, Sep/Oct 2015, Jan/Feb 2017, and Aug 2018, from various deep field observations taken as part of MUSE GTO programs, spanning the bulk of the observations. Once created, we can subtract this sky-flat from each of the science exposures in detector-coordinates at the pixtable level. For those cases where the sky-flats did not perform well, we decided to mask instead the regions with imperfect flat-fielding, again in the pixtable before resampling. Further we masked in the pixtable in rare cases individual slices with problems (e.g. due to some problem with the sky subtraction) and satellites which were identified from white-light images create from a first pass reduction.

A datacube is then created from the skyflat corrected pixtables with the pipeline recipe `scipost`, using the default 3D drizzling interpolation process. We resampled all exposures of a field individually specifying a common output WCS. We then performed quality control for each exposures, including measurements of the PSF and flux. Exposures where the flux calibration was off, e.g. due to clouds, or which had a significantly worse seeing than the majority of the exposures in the field, were rejected.

With the offsets between exposures to correct for the de-rotator wobble, computed on white-light images constructed from the pixtables, we produced data-cubes resampled to the same WCS pixel grid for each exposures. These individual data-cubes are finally combined using MPDAF (Piqueras et al. 2019). This allows one to perform an inverse-variance weighted average over a large number of data-cubes. A 3-5σ rejection (depending on the number of exposures) of the input pixels was applied in the average, to remove remaining badpixels and cosmic rays.

The combined datacube is finally processed using the Zurich Atmospheric Purge (ZAP Soto et al. 2016) version 2.0 [3] described in Bacon et al. (2021, Appendix B.3), which performs a subtraction of remaining sky residuals based on a Principal Component Analysis (PCA) of the spectra in the background regions of the datacube. We provide as input to ZAP an object mask generated from the white-light image of the combined cube with SExtractor (Bertin & Arnouts 1996) in order to remove the fluxes from all the bright objects.

The cubes were corrected for galactic extinction using the all-sky thermal dust model from the Planck mission (Planck Collaboration et al. 2014). Specifically, we used the dustmaps Python interface (Green 2018) [4] to get the galactic color excess $E(B-V)$ from Planck data. We then corrected the cube using the Cardelli et al. (1989) extinction curve with $R_V = 3.1$. This ensures that all spectra and flux measurements in the catalogs will be properly dust corrected. This cube is referred to as `beta` dataset.

In addition, we also produced a version of the cube after subtracting the QSO PSF using Pampelmuse [5] (Kamann et al. 2013) for the non-AO fields and using the Modelisation of the Adaptive Optics PSF in Python tool MAOPPY [6] (Fétick et al. 2019) for the fields taken with AO. This cube is referred to as the `psfsub` dataset.

3.2. UVES quasar spectra

The quasars of this MUSE GTO-Program were all observed with the high-resolution spectrograph UVES (Dekker et al. 2000) between 2014 and 2018 (see Tab. 3). The settings used in our observations were chosen in order to cover the

[3] `https://zap.readthedocs.io/en/latest/`
[4] `https://dustmaps.readthedocs.io/en/latest/index.html`
[5] `https://pampelmuse.readthedocs.io/en/latest/`
[6] `https://github.com/rfetick/maoppy`

Table 1: MEGAFLOW quasars fields.

ID[a]	Field name[b]	R.A. (J2000)[c]	Dec (J2000)[d]	$E(B-V)_{gal}$[e]	z_{QSO}[f]	m_r[g]	N_{abs}[h]	$N_{abs,tot}$[i]
11	J0014−0028	00:14:53.36	-00:28:27.7	0.053	1.927	19.4	3	7
12	J0014+0912	00:14:53.21	+09:12:17.7	0.210	2.308	18.5	3	13
13	J0015−0751	00:15:35.18	-07:51:03.1	0.038	0.875	19.3	3	3
14	J0058+0111	00:58:55.76	+01:11:28.6	0.025	1.222	18.2	2	3
15	J0103+1332	01:03:32.31	+13:32:33.6	0.036	1.663	18.6	3	5
16	J0131+1303	01:31:36.45	+13:03:31.1	0.067	1.595	18.6	4	7
17	J0134+0051	01:34:05.77	+00:51:09.4	0.025	1.519	18.4	4	8
18	J0145+1056	01:45:13.11	+10:56:26.7	0.068	0.938	19.1	3	5
19	J0800+1849	08:00:04.55	+18:49:35.1	0.034	1.294	17.9	4	7
20	J0838+0257	08:38:52.05	+02:57:03.7	0.028	1.770	17.8	5	8
21	J0937+0656	09:37:49.59	+06:56:56.3	0.044	1.814	19.3	3	4
22	J1039+0714	10:39:36.67	+07:14:27.4	0.040	1.532	19.3	3	5
23	J1107+1021	11:07:42.74	+10:21:26.3	0.026	1.925	17.6	6	10
24	J1107+1757	11:07:35.26	+17:57:31.5	0.022	2.133	18.9	3	8
25	J1236+0725	12:36:24.39	+07:25:51.5	0.022	1.605	18.7	4	4
26	J1314+0657	13:14:05.62	+06:57:22.0	0.031	1.880	18.0	4	4
27	J1352+0614	13:52:17.67	+06:14:33.2	0.027	1.798	18.3	3	3
28	J1358+1145	13:58:09.49	+11:45:57.6	0.021	1.484	18.0	4	4
29	J1425+1209	14:25:38.06	+12:09:19.2	0.027	1.618	18.5	4	6
30	J1509+1506	15:09:00.12	+15:06:34.8	0.030	2.238	19.3	3	4
31	J2137+0012	21:37:48.44	+00:12:20.0	0.063	1.669	18.3	4	5
32	J2152+0625	21:52:00.04	+06:25:16.4	0.060	2.389	19.4	4	4
Total							79	127

Notes. [a] ID of the field [b] QSO short name. [c] Right ascension of the QSO [hh:mm:ss; J2000]. [d] Declination of the QSO [dd:mm:ss; J2000]. [e] Color excess from the Galactic extinction at the position of the QSOs. [f] QSO redshift z_{QSO}. [g] QSO r magnitude. [h] Number of Mg II absorptions N_{abs} from the SDSS catalog of Zhu & Ménard (2013). [i] Total number of Mg II absorptions N_{abs} in the UVES data (see § 4.1).

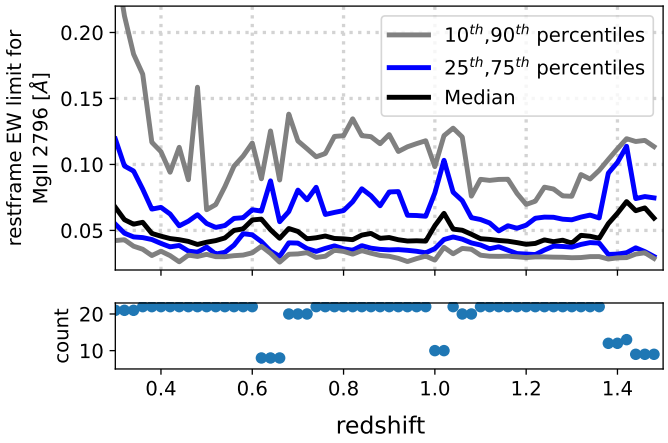

Fig. 3: The solid black line represents the median 3σ REW limits for Mg II 2796 as a function of redshift for all 22 UVES spectra. The blue and grey lines represent the 25th and 75th percentiles, respectively. Fig. A.1 shows the REW limits for each field individually. The bottom graph shows the number of sight-lines covering each redshift.

Mg II$\lambda\lambda$2796, 2803 absorption lines as well as other elements such as Mg Iλ2852, Fe IIλ2586 when possible. Additional observations were carried out in cycle 108 (2021, 2022) to fill some gaps in redshift coverage for certain sight lines and in particular weak ions. The total observing time amounts to 59 hr (63 hr, including archival observations from 2004).

The data were taken under similar conditions resulting in a spectral resolving power of R $\approx$ 38000 dispersed on pixels of $\approx$1.3 km s^{-1}. The Common Pipeline Language (CPL version 6.3) of the UVES pipeline was used to bias correct and flat field the exposures and then to extract the wavelength and flux calibrated spectra. After the standard reduction, the custom software UVES Popler (Murphy 2018, version 1.05 from Sept. 2020) was used to combine the extracted echelle orders into single 1D spectra in vacuum wavelength. The continuum was fitted with low-order polynomial functions Murphy et al. (2019).

Figure 3 shows the median 3-σ W_r^{2796} limit as a function of redshift for the 22 quasar spectra (black line). The gray lines represent the 10th and 90th percentiles, while the blue lines represent the 25th and 75th percentiles. The W_r^{2796} limits are obtained from the uncertainty per pixel σ_{pix}, the average line width of weak Mg II$\lambda\lambda$2796, 2803 w_{MgII} = 5 km s^{-1}, the pixelsize pix = 1.3 km s^{-1}, the local pixel width dl in Å and the detection significance = 3 using

$$W_r^{2796}\text{limit} = \sigma_{pix} \times \sqrt{\frac{w_{MgII}}{pix}} \times \frac{dl}{1+z} \times 3. \quad (1)$$

4. Catalogs

In this section, we present the making of the absorption line catalogs (§ 4.1) and of the galaxy catalogs (§ 4.2).

Table 2: Summary of MUSE observations for the 22 fields.

Field name[a]	T_{exp}[b]	ESO program IDs[c]	Instrument Modes[d]	PSF[e]
J0014−0028	10.0	095.A-0365(A), 096.A-0164(A), 0100.A-0089(B), 0101.A-0287(A), 0102.A-0712(A)	NOAO-N,AO-N	0.61
J0014+0912	3.0	094.A-0211(B)	NOAO-N	0.84
J0015−0751	3.3	096.A-0164(A), 097.A-0138(A), 099.A-0059(A)	NOAO-N	0.75
J0058+0111	3.1	096.A-0164(A), 097.A-0138(A), 0101.A-0287(A), 0102.A-0712(A)	NOAO-N,AO-N	0.70
J0103+1332	3.7	096.A-0164(A),0100.A-0089(A)	NOAO-N,AO-N	0.75
J0131+1303	3.7	094.A-0211(B),099.A-0059(A)	NOAO-N	0.81
J0134+0051	3.6	096.A-0164(A), 097.A-0138(A), 099.A-0059(A)	NOAO-N	0.78
J0145+1056	3.3	096.A-0164(A), 097.A-0138(A), 0100.A-0089(A),0100.A-0089(B)	NOAO-N,AO-N	0.69
J0800+1849	2.0	094.A-0211(B)	NOAO-N	0.56
J0838+0257	3.3	096.A-0164(A),098.A-0216(A)	NOAO-N	0.54
J0937+0656	11.2	095.A-0365(A), 0100.A-0089(B), 0100.A-0089(A), 0101.A-0287(A)	NOAO-N,AO-N	0.72
J1039+0714	3.3	097.A-0138(A),098.A-0216(A)	NOAO-N	0.72
J1107+1021	3.3	096.A-0164(A),098.A-0216(A)	NOAO-N	0.71
J1107+1757	2.0	095.A-0365(A)	NOAO-N	0.88
J1236+0725	5.0	096.A-0164(A),0100.A-0089(A),0101.A-0287(A)	NOAO-N,AO-N	0.73
J1314+0657	1.7	097.A-0138(A)	NOAO-N	0.53
J1352+0614	3.6	099.A-0059(A),0100.A-0089(A),0101.A-0287(A)	NOAO-N,AO-N	0.69
J1358+1145	3.1	097.A-0138(A),0100.A-0089(A)	NOAO-N,AO-E	0.55
J1425+1209	2.7	097.A-0138(A),0100.A-0089(A)	NOAO-N,AO-N	0.72
J1509+1506	2.5	099.A-0059(A),0100.A-0089(A)	NOAO-N,AO-N	0.50
J2137+0012	5.6	094.A-0211(B),0102.A-0712(A)	NOAO-N,AO-N	0.96
J2152+0625	2.0	094.A-0211(B)	NOAO-N	0.57

Notes. [a] QSO short name. [b] Total exposure time [hr]. [c] ESO program IDs of the MUSE observations. [d] Instrument mode used (AO/no-AO). [e] FWHM of the PSF at 7000Å.

Table 3: Summary of UVES observations for the MEGAFLOW fields.

QSO field[a]	UVES Grating[b]									ESO program IDs
	346	390	437	520	564	580	600	760	800	
J0014−0028	-	2.5	-	-	2.5	-	-	-	-	096.A-0609(A)
J0014+0912	-	0.8	1.7	-	0.8	-	-	1.7	-	098.A-0310(A) 096.A-0609(A)
J0015−0751	-	3.3	-	-	3.3	-	-	-	-	098.A-0310(A)
J0058+0111	-	0.8	0.8	-	0.8	-	-	0.8	-	098.A-0310(A)
J0103+1332	-	2.5	-	-	2.5	-	-	-	-	098.A-0310(A)
J0131+1303	-	1.7	-	-	-	1.7	-	-	-	096.A-0609(A)
J0134+0051	4.0	0.8	1.6	-	4.0	0.8	-	1.6	-	074.A-0597(A) 098.A-0310(A)
J0145+1056	-	3.3	-	-	3.3	-	-	-	-	096.A-0609(A) 097.A-0144(A) 098.A-0310(A)
J0800+1849	-	1.6	-	1.7	1.6	-	-	-	-	108.22KC.001 096.A-0609(A)
J0838+0257	-	0.8	-	-	0.8	-	0.8	-	-	098.A-0310(A) 096.A-0609(A)
J0937+0656	-	2.5	-	-	2.5	-	-	-	-	096.A-0609(A)
J1039+0714	2.5	2.5	-	-	2.5	2.5	-	-	-	097.A-0144(A) 108.22KC.001
J1107+1021	-	3.3	-	-	1.6	1.7	-	-	-	096.A-0609(A) 108.22KC.001
J1107+1757	-	3.3	2.5	-	3.3	-	-	2.5	-	108.22KC.001 096.A-0609(A)
J1236+0725	-	-	1.7	-	-	-	0.8	1.7	-	097.A-0144(A) 096.A-0609(A)
J1314+0657	-	0.8	-	-	0.8	-	-	-	-	097.A-0144(A)
J1352+0614	-	1.9	0.8	-	1.9	-	-	0.8	-	108.22KC.001 097.A-0144(A)
J1358+1145	0.8	0.8	-	-	0.8	-	-	-	0.8	097.A-0144(A)
J1425+1209	-	0.8	-	0.8	0.8	-	-	-	-	097.A-0144(A)
J1509+1506	-	2.5	-	-	2.5	-	1.7	-	-	108.22KC.001 097.A-0144(A)
J2137+0012	-	1.7	-	-	1.7	-	-	-	-	293.A-5038(A)
J2152+0625	-	2.5	-	2.5	-	2.5	-	-	-	293.A-5038(A)

Notes. [a] Field short name. [b] Exposure time per grating [hr]. [c] ESO program IDs of the UVES observations.

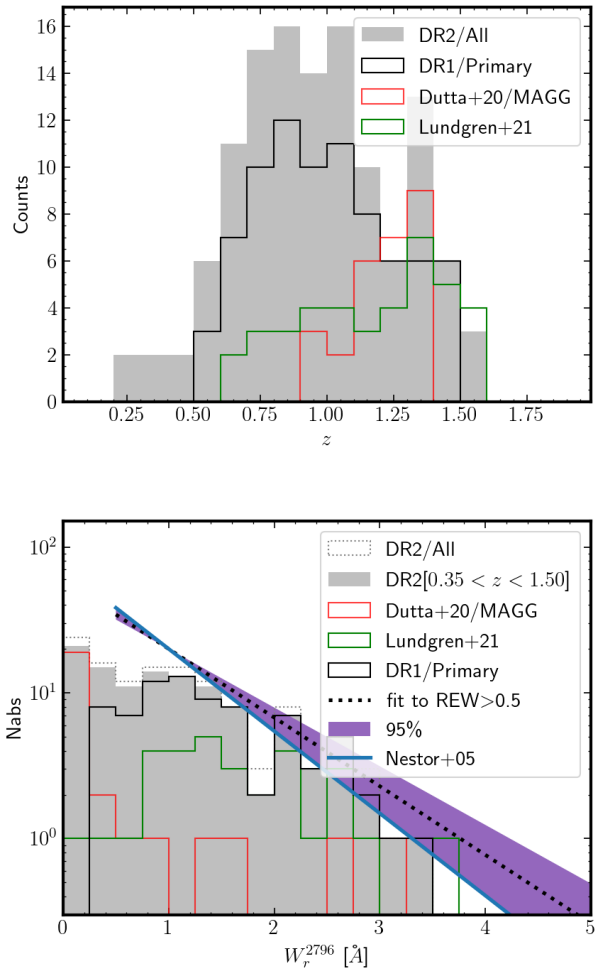

Fig. 4: *Top*: Redshift distribution of the Mg II absorption systems. The solid and gray histograms show the absorbers for the SDSS (DR1) and UVES (DR2) selections, respectively. *Bottom*: Rest-frame equivalent width W_r^{2796} distribution of the Mg II absorption systems. The dashed histogram shows the full sample of DR2 absorbers, while the solid and gray histograms represent the absorbers for the SDSS (DR1) and UVES (DR2) samples, respectively, over the same redshift interval $0.35 < z < 1.5$. In order to compare the slope of the W_r^{2796} distribution to random QSO field, we show the REW distribution from Nestor et al. (2005) (solid line) at $z = 1$ (normalization arbitrary). For $W_r^{2796} > 0.5$ Å, the 95% confidence interval of the REW slope is shown (tied to $W_r^{2796} = 1$ Å). The Mg II REW distribution in MEGAFLOW is not different than from random QSOs for strong Mg II absorptions. In both panels, the red (green) histogram represents the Mg II sample from Dutta et al. (2020) (Lundgren et al. 2021), respectively.

4.1. Mg II absorption lines

As discussed in § 2, the SDSS survey selection (DR1) yielded 79 Mg II absorption lines in the 22 QSO fields selected from SDSS spectra which we will refer to as 'DR1' absorber sample and these were used in past papers such as Schroetter et al. (2019), Zabl et al. (2019) and Wendt et al. (2021). In addition, we searched for serendipitous Mg II absorbers in our UVES spectra, and found an additional 48 Mg II absorption lines, leading to a total of 127 Mg II absorption lines, which is referred as the 'DR2' sample.

The additional absorption lines were found independently by the two members of the team (IS and SM). First, the wavelength array of each spectrum is shifted by the rest-frame wavelength ratio (2796.3543/2803.5315) of the Mg II doublet. The shifted spectrum is then plotted on top of the original spectrum. Such a shift will translate the absorption corresponding to the weaker member of the doublet (Mg II 2803) to the location of the stronger member (Mg II 2796), since the ratio of observed wavelengths is equal to the ratio of the rest-frame wavelengths, it is independent of redshift. We take a note of such coincidences in each spectrum, and determine their redshifts. We then make velocity plots for each of these putative Mg II systems to verify the presence/absence of other prominent transitions such as the Fe II, Ca II, Mn II, and C IV. However, the presence of these absorption lines was not mandatory for an absorber to be deemed as Mg II. The final Mg II catalog was then built by mutual agreement between IS and SM, considering the factors such as the detection significance, velocity structures of the two transitions, and contamination.

The final Mg II absorption catalog (DR2) contains 127 Mg II absorption lines and the list can be found on the `AMUSED` [7] and MEGAFLOW [8] websites.

Figure 4 (top) compares the redshift distribution of the full Mg II absorption line sample (grey histogram) to the pre-selected absorption lines (solid histogram). Figure 4 (bottom) compares the rest-frame equivalent width (REW) W_r^{2796} Mg II distributions of the full sample (dotted histogram) to the SDSS pre-selected sample (solid histogram). The grey histogram represents the DR2 sample after matching the redshift distribution of the DR1 sample. For comparison, the Nestor et al. (2005) and Zhu & Ménard (2013) power-laws for the REW distribution of $z = 1$ Mg II are shown (normalization is arbitrary). The dotted line represents a fit to the DR2 sample at $0.4 < z < 1.5$ and for REW greater than $W_r^{2796} \geq 0.6$ Å, along with its 95% confidence interval obtained from 5000 bootstrap fits. The MEGAFLOW Mg II absorption lines REW distribution has the same slope as random QSO fields, albeit with a different normalization as pointed in Schroetter et al. (2021) (their Fig. A.3). Indeed, the MEGAFLOW $\partial N/\partial W_r \propto \exp(-W_r/a)$ with $a = 0.86^{+0.15}_{-0.15}$ which is consistent with $a = 0.77 \pm 0.01$ from field statistics (Nestor et al. 2005; Abbas et al. 2024) for strong absorbers.

4.2. Galaxies

In this Sect. 4.2.1, we discuss the DR1 catalog of [O II] emitters associated with the 79 Mg II absorption lines in § 4.2.1. The DR1 catalog is the basis of the analysis in Schroetter et al. (2019), Zabl et al. (2019), Zabl et al. (2020), Zabl et al. (2021), Wendt et al. (2021) and Freundlich et al. (2021). In Sect. 4.2.2, we discuss our DR2 catalog of all galaxies, which consists of a dual selection of [O II] line emitters and continuum-selected sources at all redshifts. A preliminary version of this catalog was used in the analysis presented in Langan et al. (2023) and Cherrey et al. (2024).

[7] `https://amused.univ-lyon1.fr/project/megaflow/`
[8] `https://megaflow.univ-lyon1.fr/data`

4.2.1. DR1: [O II] emitters at $z_{\rm abs}$

As discussed in Zabl et al. (2019), the redshift identification of galaxies associated to the 79 Mg II absorption lines was based on multiple pseudo narrow-band (NB) images of width $\approx$ 400 km s^{-1} [9] suitable for [O II], [O III] and Hβ emitters extracted from an early data reduction of the dataset (Zabl et al. 2019). Each NB image is continuum subtracted by using two off-bands, and the NB images are combined in a single NB image (S/N weighted). We then automatically search for low-S/N objects in these NB images using the detection algorithm SExtractor (Bertin & Arnouts 1996). We also searched for quiescent galaxies by creating pseudo-NB images around the Ca H&K doublet. We ran SExtractor on the inverted NB image given that quiescent galaxies at the right redshift have negative fluxes in the continuum-subtracted images. Finally, we manually checked each candidate. This procedure consisted in a sample of 168 galaxies associated to the 79 absorbers, which is referred to as the 'DR1' galaxy sample.

4.2.2. DR2: blind [O II] emitters

With $\sim$ 90,000 optical spectra per single pointing, there is demand for automatic source detections such as the Line Source Detection and Cataloging (LSDCat) algorithm (Herenz & Wisotzki 2017) or the ORIGIN software (Mary et al. 2020). LSDcat is a matched filtering and thresholding algorithm for emission lines algorithm written for IFU data and used for single emission lines such as Lyα emission lines. After the filtering the elements in the data cube represent the statistical S/N an emission line at that voxel position would have given that it was perfectly represented by the filter template and also assuming fully Gaussian, uncorrelated noise. The resulting signal is quite robust against varying spectral or spatial sizes of the single-line template. Hence, LSDcat was also quite effective at indicating other emission features than pure Lyα. A simple 'thresholding-approach', however, is prone to spurious detections, so-called false positives directly depending on the threshold.

Here, we use the Find Emission LINE objects (FELINE [10]) algorithm from Wendt et al. (submitted) which combines a fully parallelized galaxy line template matching with the matched filter approach for individual emission features of LSDcat. For the 3D matched filtering, the complete data cube is first median filtered to remove all continuum sources, and then cross-correlated with a template of an isolated emission feature in two spatial and one spectral dimension. We assumed a simple Gaussian with a FWHM of 250 km/s for the line profile and a PSF based on the given seeing in the data cube.

The FELINE algorithm then evaluates the likelihood in each spectrum of the cube for emission lines at the positions provided by a given redshift and a certain combination of typical emission features. FELINE probes all possible combinations of up to 14 transitions paired in 9 groups: Hα, Hβ, Hγ, Hδ, [O II], [O III], [N II], [S II], and Ne III for the full redshift range of interest ($0.4 < z < 1.4$). This particular selection of lines is motivated by the most prominent emission features expected in the MUSE data within this redshift range. This results in 512 (2^9) different models that are assessed at roughly 8,000 different redshifts for each of the $\approx$ 90,000 spectra in a single data cube. To ensure that only lines above a certain S/N threshold contribute to each model, a penalty value is subtracted for each additional line. The S/N near strong sky lines are set exactly to that threshold. Hence lines that fall onto such a contaminated region will not affect model quality. This is particularly useful for doublet lines that then contribute to a model even when one of the lines aligns with a skyline. For each spaxel the model with the highest accumulative probability over all contributing lines and its corresponding redshift are determined. This approach has the benefit to pick up extremely weak emitters that show multiple emissions lines while avoiding the deluge of false positives when looking for single lines below a certain S/N threshold. This can be applied to each spatial element independently and was thus fully parallelized. From the resulting spatial map of best model probabilities, the peaks were automatically selected via maximum filter and 1D spectra were extracted for each emission line galaxy candidate. Those extracted spectra are fitted with an emission line galaxy template and with the redshift as well as the individual line strengths as only free parameter to reach sub pixel accuracy in an early redshift estimate as well as deriving further diagnostics for the later manual inspection, such as the [O II] line ratio.

Several of us (JZ, IS, SM, MW, NB) visually inspected the FELINE solutions with a custom tool and rated each object according to the likelihood of being an [O II] emitter. The score was 'A' for a clear identification of an [O II] emitters, 'B' for likely [O II] emitters (due to weak S/N or marginally [O II] doublet resolved), and 'No' for real objects other than [O II] emitters. A special flag 'X' was used when the redshift solution was wrong or needed to be discussed/resolved. The scores (A/B/No/X) were converted to numerical values (2/1/0/-9) and averaged. The list of FELINE sources (along with masks) with their average (and dispersion) scores makes the FELINE data products.

4.2.3. DR2: continuum sources

We use SExtractor (Bertin & Arnouts 1996) on the white-light images extracted from each datacube to identify continuum-selected sources. For each field, we optimized the detection parameters. Typically, we used a minimum area of 6 to 8 spaxels, a S/N threshold $\approx$ 1.0–1.3, a Gaussian kernel of FWHM 2 spaxel, a deblending threshold of 64 levels, and an automatic background subtraction.

4.3. Completeness

We estimated the completeness of our data by adding $N = 150$ fake [O II] emitters in two versions of one of our MUSE fields (J0937p0656), using a shallow (2.3 hr) and the deepest (11.2 hr) version. The [O II] emitters were placed at 5 wavelengths far from sky emission lines ($\sim$505, 605, 705, 820 and 920nm) and spatially away from known sources. The emitters are generated using the GalPaK^{3D} algorithm using the measured PSF and with realistic galaxy parameters for [O II] emitters covering a range of redshifts, inclinations, fluxes and surface brightnesses. Specifically, we used an inclination i selected according to a uniform distribution $\sin(i) \propto \mathcal{U}(0.5, 0.95)$ over the range $i = [30, 75]$ deg; posi-

[9] This filter width gives the optimal S/N for [O II]$\lambda\lambda$3727,3729 doublet assuming a line width of FWHM$\approx$ 50 km s^{-1}.
[10] `https://github.com/enthusi/feline`.

tion angles uniformly from $\mathcal{U}(0, 360)$; a (turbulent) velocity dispersion $\sigma_0 = 25$ km s^{-1}; a tanh rotation curve with $V_{\rm max} = 100$km s^{-1} and turn-over radius of $r_v = R_e/1.26$ (following Amorisco & Bertin 2010; Bouché et al. 2015); half-light sizes R_e of 2.5 and 5 kpc; [O II] doublet ratios randomly selected from a normal distribution $\mathcal{N}(0.8, 0.1)$; flux profiles with Sérsic index $n = 1$; and total fluxes of [1, 2, 4, 6, 8, 10] $\times 10^{-18}$ erg s^{-1} cm^{-2}.

We ran FELINE on the shallow and deep cubes with fake sources, and the completeness function $f_{\rm c}$ is then defined as the fraction of sources detected. Because $f_{\rm c}$ is a complex function of 3D surface brightness in x, y and wavelength, it traditionally requires generating a large number of fake sources (over several detection runs), which then requires binning the results in wavelength, sizes, flux, etc. Instead, we used the Bernoulli regression suitable for binary outcome developed in Bouché & McConway (2019) and presented in Schroetter et al. (2021) which has the advantage that it requires no binning of the data. Briefly, for a set of fake sources, the detectability Y_i is either 0 or 1, and the method consists in parametrizing the completeness function f_c, which ranges from 0 to 1, as a Logistic function $L(t) \equiv 1/[1+\exp(-t)]$ where the function $t = F(X_i; \theta)$ is any linear combination of the independent variables X_i, $t = \alpha+\beta_1 X_1+\cdots+\beta_n X_n$. The Bayesian algorithm then optimizes the parameters using a Bernoulli likelihood against the observed series of detected/undetected sources Y_i. We use the NUTS (No-U-Turn Sampler from Hoffman & Gelman 2014), a self-tuning Hamiltonian Monte Carlo, implemented in the python probabilistic package PYMC3 (Salvatier et al. 2016). For the logistic function L, we use F as a function of flux f, size R, and wavelength λ, namely:

$$F(X_i; \theta) = A[\log f_i + {\rm ZP}(\lambda)] + B(\log R_i - \log \overline{R}) \quad (2)$$

where A defines the sharpness of the Logistic function $L(t)$, B the size dependence, and ZP(λ) the wavelength dependent 50% completeness taken as a third order polynomial ${\rm ZP}(\lambda) = C + \alpha(\lambda - \lambda_0) + \beta(\lambda - \lambda_0)^2 + \gamma(\lambda - \lambda_0)^3$ where $\lambda_0 \equiv (1 + z_0) \times 3727$ Å the reference wavelength for [O II] emitters at redshift $z_0 = 1$.

Figure 5 shows the completeness achieved for [O II] emitters in the J0937+0656 data as a function of wavelength/redshift (panel a) and as a function of flux and size (panel b). The fitted parameters are listed in Table 4 which indicates that the 50% completeness for [O II] emitters at $\lambda_0 \approx 7000$ Å is $3.7^{+0.8}_{-0.6} \times 10^{-18}$erg s^{-1} cm^{-2} ($7.07^{+1.6}_{-1.3} \times 10^{-18}$erg s^{-1} cm^{-2}) in the deep (shallow) cubes.

Regarding the completeness of continuum sources we estimate the completeness from the number counts (N/deg^2/0.5mag) shown in Fig. 6(left). By fitting the F775W number counts normalized to the expected counts from large galaxy surveys such as the recent GAMMA/DEVILS survey (Koushan et al. 2021), we find that the 50% completeness is $m_{F775W} \approx 25.2$ m$_{\rm AB}$ the shallow fields (2-4hr) and is $m_{F775W} \approx 26$ m$_{\rm AB}$ for the two deep fields (11hr).

4.4. Source inspection

At this point each source in the FELINE and continuum-based catalogs are assigned a 6-digit `FELINE_ID` or `WHITE_ID` using the following nomenclature: 'xxa001' where 'xx' is the unique field ID (Table 2) and 'a' is 0 for FELINE source, 1 for continuum sources or 2 for continuum sources near the QSO, in the `psfsub` dataset.

Following Bacon et al. (2023), we use the PYMARZ software (Hinton et al. 2016) in order to identify five redshift solutions for the FELINE and continuum sources with 9 templates for passive and star-forming galaxies and then used PYPLATEFIT [11] in order to perform emission and absorption line fitting on each of the redshift solution. We also computed the narrow-band images associated with each emission or absorption lines with $S/N > 2$ packaged in 'source' fits files, which are important to assess the detection of weak lines. The FELINE, PYMARZ redshift solutions, the fitted lines with $S/N > 2$, the narrow-band images and spectra

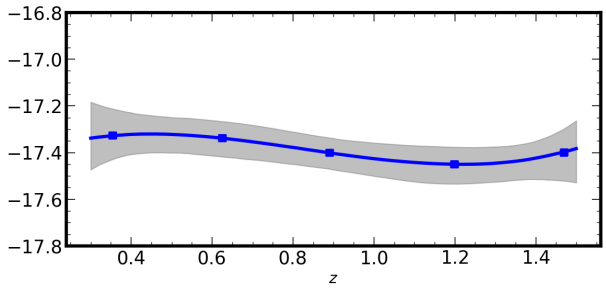

(a)

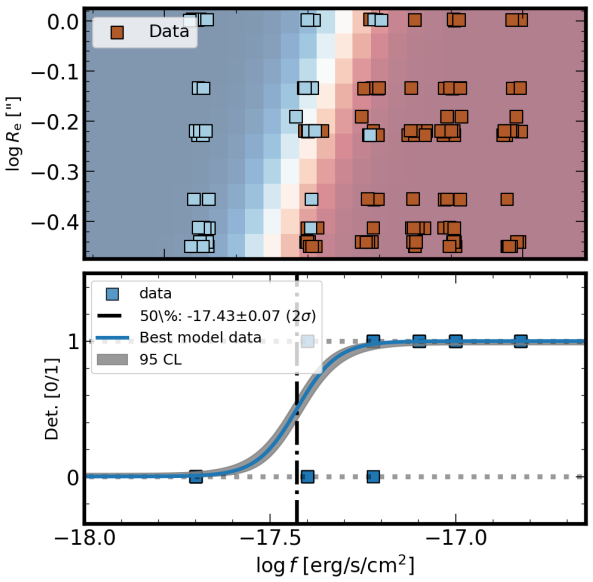

(b)

Fig. 5: Completeness for [O II] emitters in the deep cube J0937+0656. (a) Completeness level (50%) as a function of redshifts. (b) Completeness as a function of size $R_{\rm e}$ (top panel) and [O II] fluxes (bottom panel). The red/blue squares represent the [O II] emitters detected (not detected), respectively. The shaded area represents the fit to the unbinned data.

[11] A python-inspired version of the PLATEFIT IDL code (Brinchmann et al. 2004).

Table 4: Parameters from the completeness as a function of flux, size, and redshift (see Eq. 2). Errors are 2σ (95%).

cube	A	B	C	α	β	γ
2.3hr	$11.69^{+4.45}_{-3.48}$	$-9.66^{+5.25}_{-5.86}$	$-17.15^{+0.09}_{-0.09}$	$-0.05^{+0.30}_{-0.32}$	$-0.16^{+0.54}_{-0.54}$	$-0.17^{+1.20}_{-1.18}$
11hr	$18.45^{+5.84}_{-5.94}$	$-8.57^{+6.68}_{-7.45}$	$-17.43^{+0.07}_{-0.08}$	$-0.20^{+0.26}_{-0.27}$	$0.29^{+0.46}_{-0.46}$	$0.58^{+1.02}_{-1.05}$

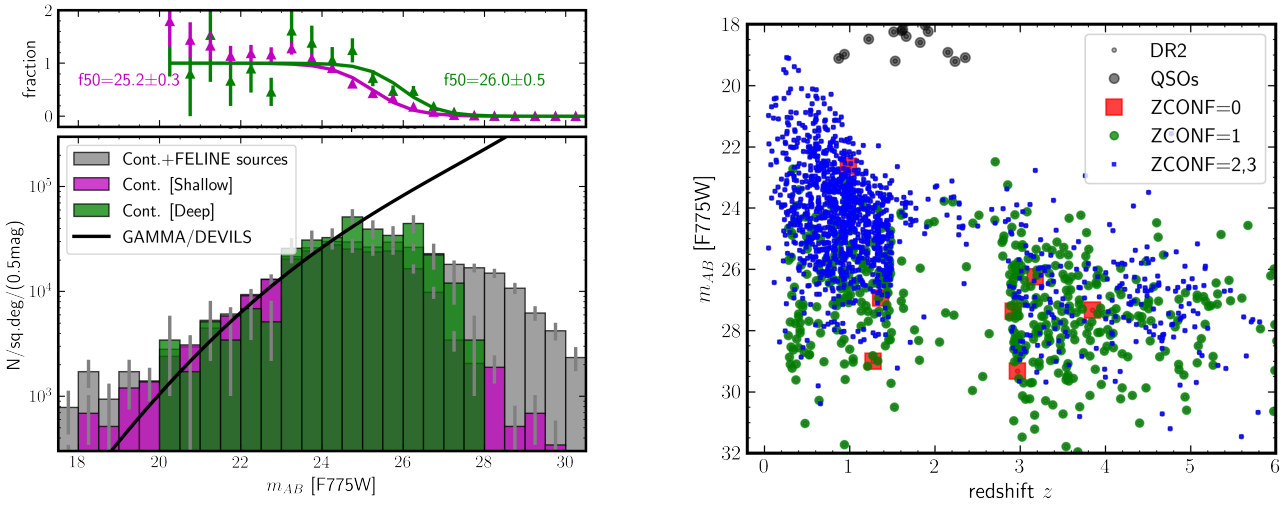

Fig. 6: *Left:* Magnitude F775W number counts. The grey histogram represents the entire MEGAFLOW survey. The magenta histogram represents the 20 shallow fields and the green histogram the 2 deep fields. Compared to the number counts from the GAMMA/DEVILS survey (Koushan et al. 2021), the MEGAFLOW survey is 50%-complete to $i \approx 25.2$ m_{AB} (26 m_{AB}) in the shallow (deep) fields, respectively. *Right:* Magnitude-redshift distribution of all sources with redshifts $z > 0$. The QSOs are shown as grey circles. The galaxies with `ZCONF`= 1 (2,3) are represented as green circles (blue squares), respectively.

are all used to produce static html files as in Bacon et al. (2023, their Fig.19).

These static html files are then fed into a modified version of the SourceInspector tool (Bacon et al. 2023), a python-Qt interface that allow users to select one of the redshift solutions or to provide a new one. But most importantly, the SourceInspector tool allows the user to match continuum-detected sources with FELINE-detected sources and vice-versa with confidence.

4.5. Categories for inspection

In order to be highly complete, at this stage, the catalog contains a high fraction of false detections. In order to optimize the time required for inspecting the catalogs with SourceInspector, we pre-matched the FELINE and continuum sources and focus on galaxies at $0.4 < z < 1.4$ which are likely either star-forming galaxies with [O II] or passive galaxies with just continuum. Specifically, we cross-matched the FELINE and continuum catalogs according to their RA, DEC and defined the following categories:

- 1.1 'GoodFelineCont' Sources with FELINE score ≥ 1.0 and continuum detection;
- 1.2 'GoodFelineNoCont' Sources with FELINE score $\geq$ 1.0 and no continuum detection;
- 1.3 'GoodFelineNoMarz' Sources with FELINE score$\geq$ 1.0 whose redshift is not among the 5 Marz solutions within 150 km/s;
- 2.1 'BrightContGoodFeline' Bright continuum sources with magAUTO$<$ 24.5 (25.0 for the two deep fields);
- 2.2 'BrightContNoFeline' Bright continuum sources without a FELINE match;
- 3.0 'FelineBorderLine' Sources with FELINE score between 0.5 and 1.5; or with a score standard dispersion > 0.45
- 4.0 'Other' Sources not in the other categories

For instance, for the deep field J0014−0028, there are 289 FELINE sources and 251 continuum sources, and they are distributed in each category as follows:

- 1.1 GoodFelineCont 66
- 1.2 GoodFelineNoCont 23
- 1.3 GoodFelineOffMarz 18
- 2.1 BrightContGoodFeline 30
- 2.2 BrightContNoFeline 31
- 3.0 FelineBorderline 46
- 4 Other (FELINE) 180; and Other (Cont) 190

Several of us (MW, IS, JZ, RB, NB, SM, JR) inspected the redshift solutions for the categories 1.x, 2.x and 3.0 with SourceInspector where each person assessed the redshift confidence – ZCONF– ranging from 0 to 3.

A confidence level of `ZCONF=0` corresponds to the situation where no redshift solution was found. A confidence level of `ZCONF=1` corresponds to a low confidence solution, i.e. when the redshift solution remains uncertain (could be [O II] or Lyα) owing to the low S/N of the line. A confidence level of `ZCONF=2` corresponds to a high S/N single

Table 5: Distribution of redshift confidence ZCONF for various classes of sources.

	ZCONF				
Class	0	1	2	3	All
QSOs	0	0	0	22	22
Stars ($z = 0$)	0	0	3	54	57
low$-z$ ($0 < z < 0.35$)	0	17	2	90	109
[O II]($0.35 < z < 1.5$)	6	173	244	734	1157
Desert ($1.5 < z < 2.8$)	0	28	20	28	76
LAE ($z > 2.8$)	7	376	276	10	669
unknown	337	0	0	0	337
All	350	594	545	938	2427

line whose shape is identifiable (e.g. a resolved [O II] doublet, an asymmetric Lyα). A confidence level of ZCONF=3 corresponds to a secure redshift with multiple lines.

4.6. Reconciliation

The results of the visual inspections were then combined and when there were several different redshift solutions proposed, we resolved the disagreement during the reconciliation meetings.

The inspection and reconciliation process also yielded some sources that required to be split (in cases where the SExtractor deblending failed) or to be merged (in cases where FELINE assigned two redshifts due to a large kinematic gradient). The entire sequence of steps in the process were processed with custom routines forming the MegaFlow Catalog Processor (MFCP) which is based on MuseX used in Bacon et al. (2023). The sequence is illustrated in Fig. 7.

As discussed in § 4.5, the entire process is optimized for galaxies at $z < 1.5$ and is somewhat biased against Lyα emitters which falls into the category '4', which was not systematically inspected.

4.7. Final DR2 catalog

The final catalog (v2.0) contains 2427 sources, which includes 22 quasars, 57 stars, 1998 galaxies with ZCONF$\geq$ 1 and 350 sources with no redshifts (ZCONF= 0). The statistics of ZCONF in the final catalog is given in Table 5 for various classes such as nearby galaxies, [O II] emitters, galaxies in the redshift desert ($1.5 < z < 2.8$) and Lyα emitters at $z > 2.8$.

Prior to performing the photometric measurements, the object masks were merged into a single mask for the sources with both FELINE and continuum detections. Note that this leads to a series of object masks which can be overlapping. For instance, the QSO source was obtained from the beta dataset, while nearby sources were obtained from the psfsub dataset, and in this situation, the small sources can be embedded into the QSO segmentation mask. The are also emission line objects that are in the foreground/background from a continuum object, in which case, the object masks can overlap significantly. As a result, we provide a is_blended flag for all sources.

Using Photutils (v1.4.0) and theses object masks, we determined the photometry for each objects in R, I, $SDSS_r$, $SDSS_i$, F775W, and 13 pseudo-medium bands (320Å wide) covering the wavelength range from 4780 to 9260 Å, excluding the laser notch filter. The magnitude–

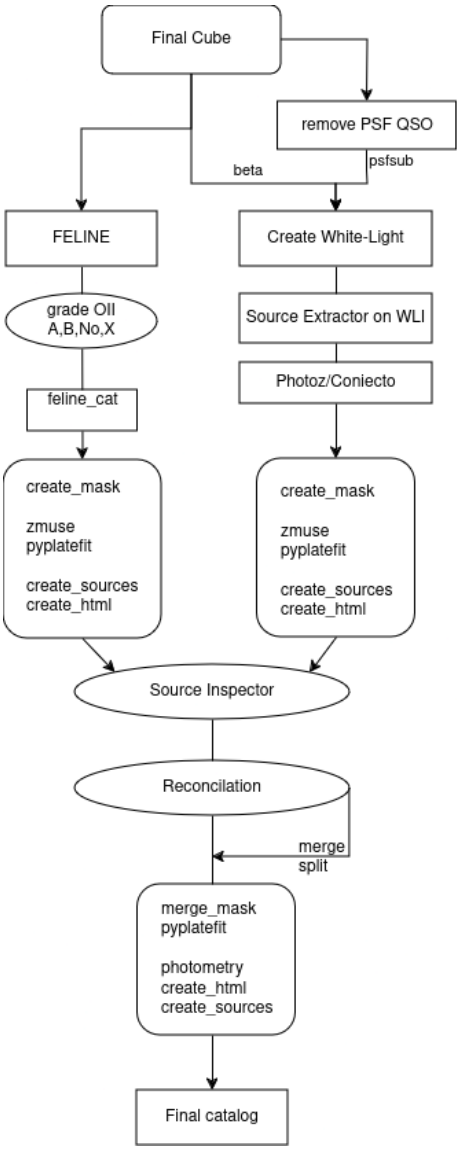

Fig. 7: Schemaric illustration of the process used to generate the final catalog from the FELINE and continuum-based catalogs.

Table 6: Magnitude (F775W) completeness limit (m_{AB}) for the deep (shallow) fields, respectively.

	50%	90%
All	26.0 (25.2)	25.0 (24.2)
ZCONF>= 1	25.7 (25.0)	24.8 (23.9)
ZCONF>= 2	25.5 (24.8)	24.7 (23.8)

redshift distribution for the 1998 galaxies in the DR2 final catalog with redshift $z > 0$ is shown in Fig. 6 (right). The graph clearly shows the redshift gap at $1.5 < z < 2.8$ due to the lack of lines between Lyα and [O II] in the MUSE wavelength range. The magnitude completeness limits as a function of redshift confidence ZCONF are given in Table 6 using the method described in § 4.3.

In section § 6.2, we compare the properties of the DR2 galaxy catalogs to the previous DR1 version.

4.8. Final DR2 data products

A final 5-digit ID was assigned to each source with the convention that 'xx001' was reserved for the QSO, where 'xx' is the field ID from Table 2. The catalog files are described in Appendix B.

We also provide new htmls and new source fits files for each object, which are available on the AMUSED interface [12] after running PyPlatefit in order to perform emission and absorption line fitting on each emission or absorption line independently. An example of a final html file is shown in Fig. B.1. The AMUSED interface is searchable and details are presented in Bacon et al. (2023).

5. Physical properties

5.1. SED stellar masses

With the photometry and the 13 pseudo-medium bands, we used a custom SED fitting code Coniecto as in Zabl et al. (2019). This code is described in Zabl et al. (2016). Briefly, we use BC03 models (Bruzual & Charlot 2003) with a delayed-τ star-formation history (SFH) and nebular line + continuum emission added following the recipe by Schaerer & de Barros (2009) and Ono et al. (2012). Here, we use a Chabrier (2003) Initial Mass Function and a Calzetti et al. (2000) extinction law. While we used the same extinction law both for nebular and stellar emission, we assume higher nebular extinction, $E_N(B-V)$, than stellar extinction, $E_S(B-V)$, with $[E_S(B-V) = 0.7E_N(B-V)]$.

Fig. 8(left) shows an example of SED fit for galaxy ID=22055 with redshift $z = 0.9856$, and stellar mass $M_\star = 10^{9.18}$ M$_\odot$ and Fig. 8 (right) shows the stellar mass-redshift distribution for the low-redshift galaxies in the DR2 catalog (grey circles). The filled squares in Fig. 8(right) show the mass-redshift distribution for the galaxies within 100 kpc of the QSO sight-lines. The histogram inset of Fig. 8 (right) shows that the Mg II host galaxies have a mean (median) stellar mass of $\log M_\star/\mathrm{M}_\odot = 9.75$ (9.67), respectively.

5.2. Star formation rates

We compute dust-corrected SFRs using the [O II] fluxes using the procedure presented in Langan et al. (2023), which is based on the empirical calibration of Gilbank et al. (2010, 2011) which incorporates the dependence of the Balmer decrement with stellar mass. Namely, we use

$$\mathrm{SFR} = \frac{\mathrm{L}_{[\mathrm{O\,II}]}/(1.12 \times 2.53 \times 10^{40} \mathrm{erg\ s^{-1}})}{a \times \tanh[(x-b)/c] + d} \quad (3)$$

where $\mathrm{L}_{[\mathrm{O\,II}]}$ is the [O II] luminosity, $x = \log M_\star$, $a, b, c = -1.424, 9.827, 0.572$ and $d = 1.70$. The factor 1.12 converts the Gilbank et al. (2010) calibration to the Chabrier (2003) IMF used throughout the survey.

5.3. Morpho-kinematics

In order to derive the morpho-kinematic of the galaxies, we use the GalPaK^{3D}algorithm (Bouché et al. 2015) which performs a forward fit of a disk model with 10 free parameters directly on the 3-dimensional MUSE data. GalPaK^{3D}takes into account the effect of the spectral line spread function (LSF) and of the point spread function (PSF) to deconvolve the observations and yields the intrinsic galaxy properties namely the main axis orientation, the inclination, the half-light radius, the redshift, the maximum velocity, the velocity dispersion, the flux and the position of the galaxy. We run GalPaK^{3D}on subcubes centered on either [O II], [O III] or Hα emission lines, with the continuum subtracted, using the PSF from § 3.1 and the LSF as in Bacon et al. (2023), namely the median LSF FWHM is $\mathrm{LSF[Å]}(\lambda) = 5.866 \times 10^{-8}\lambda^2 - 9.187 \times 10^{-4}\lambda + 6.040$ where λ is in Å.

[12] https://amused.univ-lyon1.fr/project/megaflow/

6. Results

6.1. Matching galaxies with absorbers

The association of absorption systems with their galaxy counterparts is crucial to understand the physical processes at play in the CGM. We first associate galaxies to Mg II absorption lines according to the redshift difference between the galaxy and the absorption, Δv.

Using a $\Delta v = 500$ km s^{-1}, the distribution of the number of galaxies per Mg II absorption system is shown in Fig. 9(left) for the entire MUSE FOV. One sees that there are approximately on average

$$N_{\mathrm{obs}} = 2.9 \pm 1.6 \quad (4)$$

galaxies per absorber, and as discussed in Cherrey et al. (2024), this is close to the expected mean number of galaxies which is

$$N_{\mathrm{exp}} = 3.3 \pm 3.1 \quad (5)$$

in a cylinder of radius $r_{\mathrm{max}} < 280$ kpc, (corresponding to the same area of the MUSE FOV) and height $\Delta z = 500$ km s^{-1} for galaxies in halos of mass $M_{\mathrm{h}} > 10^{11}\mathrm{M}_\odot$ using the halo mass function from Tinker & Chen (2008). Note, that the drop in Fig. 9(left) at $N = 5$ is entirely caused by the MUSE FOV.

If we restrict ourself to galaxies within an impact parameter b less than 100 kpc, the red/filled histogram in Fig. 9(right) shows the number of galaxies that are within $b < 100$ kpc around 80 strong ($W_{\mathrm{r}}^{2796} > 0.5$ Å) absorption systems. This figure shows that the majority (60 out of 80, 75%) of Mg II systems are matched with 1 or 2 galaxies, and only 10 have no counterparts.

Figure 10 shows the velocity difference (Δv) between the galaxy redshift and the absorption redshift as a function of impact parameter b. The δv standard deviation is $\sigma \sim 100$ km s^{-1}, much smaller than our search boundary of ± 500 km s^{-1}, as in Huang et al. (2021). This shows that, in spite of our search range of $|\Delta v| < 500$ km s^{-1} (solid horizontal lines), the galaxies associated with the Mg II absorbers are found within ± 200 km s^{-1} from the absorption lines and within ± 100 km s^{-1} at distances less than 50 kpc. The dotted line represents the escape velocity v_{esc} of a 10^{12} (Navarro et al. 1997, NFW) halo, and this figure indicates that the Mg II gas is not virialized as Δv decreases towards the center whereas it ought to increase as in groups (Cherrey et al. 2024) if the gas were virialized. It shows also that we are not likely affected by misassigned gas, namely within $|\Delta v| < 500$ km s^{-1} but outside the virial radius as discussed in Ho et al. (2020) in the context of the Mg II in EAGLE simulations or in Weng et al. (2024) in the context of Lyman limit systems in TNG50.

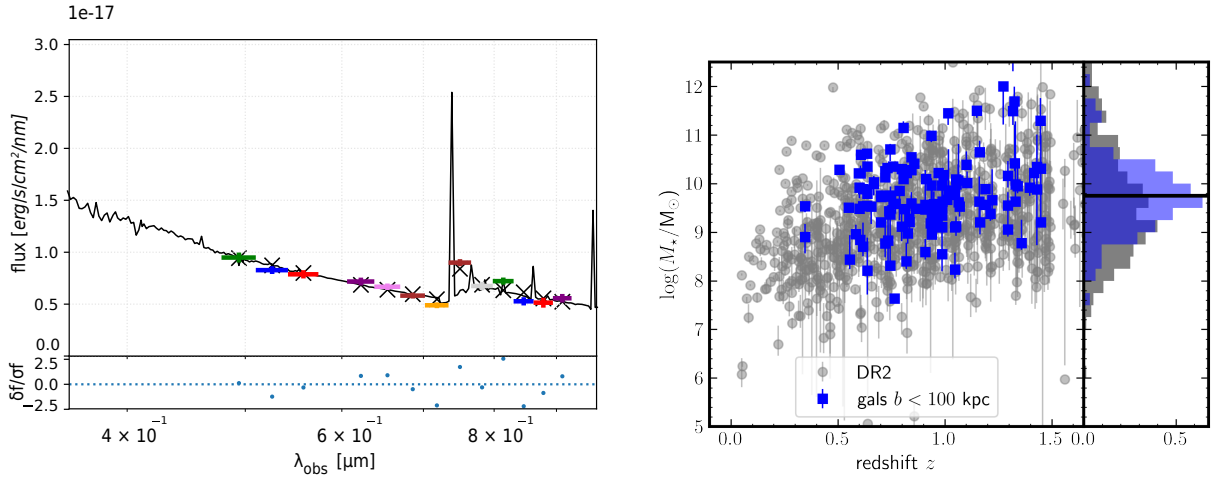

Fig. 8: *Left:* Spectral Energy Distribution (SED) for galaxy ID=22055 at $z = 0.9856$ from field J1039p0714. The black line represents the best fit template. The solid bars represent the pseudo-narrow bands. *Right:* Stellar-mass vs redshift for the galaxies in the DR2 catalog at $0.35 < z < 1.5$. The squares represent the galaxies within 500 km s^{-1} of the Mg II absorbers and with impact parameters $b < 100$ kpc. The histogram shows the normalized stellar mass distributions.

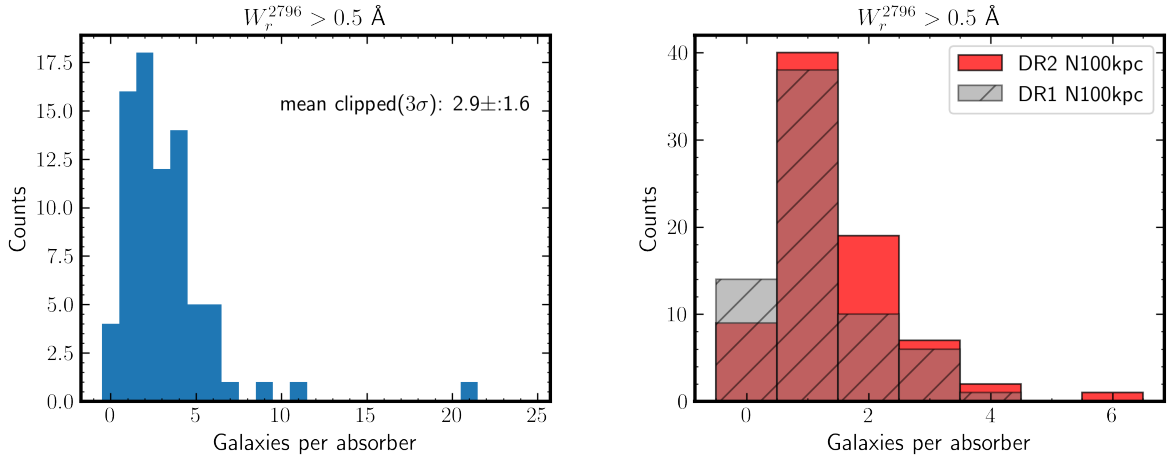

Fig. 9: *Left:* Distribution of the number of galaxies that are within ±500 km s^{-1} of strong ($W_r^{2796} > 0.5$ Å) absorption systems, within the MUSE FOV, and within the MUSE wavelength coverage for [O II] emitters, i.e. $0.35 < z_{abs} < 1.45$. The mean (median) number of galaxies is 2.9±1.6 (3.0), respectively. *Right:* The red (hashed) histogram shows the number of galaxies around strong ($W_r^{2796} > 0.5$ Å) Mg II absorption systems within 100 kpc in the redshift range $0.35 < z < 1.45$ suitable for [O II] emitters, from the DR2 (DR1) samples, respectively.

6.2. Comparison between DR1 and DR2 galaxy catalogs

A notable difference between our DR1 and DR2 galaxy catalog is that the DR1 galaxy catalog from Zabl et al. (2019) was constructed primarily from pseudo-narrow band images at the redshift of [O II] corresponding to the Mg II absorption catalog, while the final DR2 catalog is constructed such that it is totally blind to the presence of Mg II absorptions.

Out of the 80 (69) systems in DR2 (DR1), there are 115 (80) galaxies within 100 kpc associated with absorbers in the DR2 (DR1) samples, respectively. This corresponds to a 'success' rate in finding at least one galaxy of $\sim 90\%$ (see Table 7) for strong Mg II systems ($W_r^{2796} > 0.5$ Å), compared to DR1 which had $\approx 80\%$ success rate (Schroetter et al. 2019; Zabl et al. 2019).

Fig. 9(right) compares the number of galaxies per absorber within $b < 100$ kpc, for strong ($W_r^{2796} > 0.5$ Å) Mg II systems. The red (grey) histogram represents the number of galaxies per absorption lines in the DR2 (DR1) catalogs. This figure also shows that there are fewer systems (10 vs 14) without galaxies, while there are more systems (80 vs 58) with 1 or 2 galaxies.

Fig. 11 compares the properties of the DR2 and DR1 catalogs, in particular it compares the redshift, magnitude and impact parameters of the galaxies associated with Mg II absorptions at $0.3 < z < 1.5$ in the DR1 and DR2 catalogs. The difference between the red solid and hashed histogram shows the benefit from a blind approach.

6.3. Primary galaxy

Within the MEGAFLOW sample, we define *primary* galaxies as the galaxies we could unambiguously identify as re-

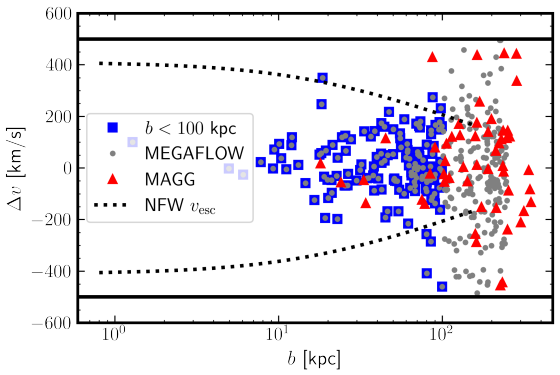

Fig. 10: Velocity offset Δv versus impact parameter b. The squares show the MEGAFLOW sample for galaxies within impact parameter $b < 100$ or b <250 kpc. The triangles represents the MAGG sample from Dutta et al. (2020). The dotted line represent the escape velocity v_{esc} for the median halo mass of isolated galaxies $M_h = 10^{11.7}$ $M_\odot$ (Cherrey et al. 2025)

Table 7: Success rate in finding the host galaxy with [O II] within the MUSE wavelength coverage, i.e. at $0.35 < z_{abs} < 1.5$.

W_r^{2796} (Å)[a]	N_{abs}[b]	$N_{100} \geq 1$[c]	$f(\%)$[d]	N_{gals}^{100}[e]
>0.2	95	74	0.78	119
>0.5	78	69	0.88	113
>0.8	64	56	0.88	89
<0.2	20	10	0.5	17
All	126	85	0.67	138

Notes. [a] Minimum Mg II REW. [b] Number of absorptions lines. [c] Number of absorptions lines with at least 1 galaxy with 100 kpc ($N_{100} \geq 1$. [d] Fraction of Mg II absorptions with $N_{100} \geq 1$. [e] Number of galaxies within 100 kpc

sponsible for Mg II absorption in quasar spectra (if any at the same redshift). We identify these primary galaxies blindly (without considering Mg II absorptions) by applying the following criteria:

- $0.3 < z < 1.5$;
- ZCONF ≥ 2;
- $z_{gal} < z_{QSO}$ with $\Delta v_{QSO} \geq 1000$ km s^{-1};
- $b < 150$ kpc;
- smallest b within ± 1000 km s^{-1}. Any neighbor must have b at least 50 kpc larger;
- $N_{FOV} < 5$ to avoid groups

with z_{gal} and z_{QSO} being respectively the redshift of the galaxy and the redshift of the quasar of the field, Δv_{QSO} being the velocity difference between the quasar and the galaxy and N_{FOV} being the number of galaxies in the MUSE field of view in a ± 1000km s^{-1} window. In total, 170 *primary* galaxies have been identified. Finally, out of the 115 absorptions in the redshift range $0.3 < z < 1.5$, 43 can unambiguously be associated with a *primary* galaxy. On the other hand 127 *primary* galaxies are not associated with any absorption.

This set of *primary* galaxies (associated / not associated with an absorption) are particularly useful to understand what are the physical parameters responsible for having an absorption at a given impact parameter.

6.4. SFR distribution

We investigate the impact of the SFR on the presence of a counterpart Mg II absorption by comparing the SFR distribution for *primary* galaxies (as described in 6.1) associated with an absorption to those not associated with an absorption. Figure 12 shows the stellar mass versus SFR, namely the main-sequence for these two sub samples. One sees that this MUSE survey is sensitive to galaxies with $M_\star \gtrsim 10^{7.5}$ and SFR $\gtrsim 0.01$ $M_\odot$ yr^{-1}, but that the majority of Mg II host galaxies have SFR> 1 $M_\odot$ yr^{-1} and $M_\star > 10^9$ $M_\odot$. This indicates that the survey would have detected satellites with mass ratio 1 : 20 or greater.

6.5. Gas density profile

Fig. 13 shows the REW impact parameter ($W_r^{2796} - b$) relation. The squares (circles) shows the relation for the *primary* galaxies with $N_{100} = 1$ ($N_{100} > 1$), respectively. In Cherrey et al. (2024), we investigate the $W_r^{2796} - b$ relation for group-selected pairs and the associated in groups. In Cherrey et al. (2025), we investigate the $W_r^{2796} - b$ relation for isolated galaxies along with its dependence with respect to SFR, mass, redshift and azimuthal angle α.

6.6. On the effect of pre-selecting sight-lines

The MEGAFLOW survey is inherently an absorption-centered survey with the pre-selection of sight-lines with Mg II absorption lines as discussed in § 2. But the wide wavelength range and hence redshift coverage ($0.3 < z < 1.5$) allows us to perform a *galaxy-centered* analysis such as the characterization of the covering fraction, namely the fraction which have a Mg II absorption above some column density or REW, of galaxies (Schroetter et al. 2021) or groups (Cherrey et al. 2024). In Schroetter et al. (2021), we investigated the covering fraction of Mg II absorptions at $1.0 < z < 1.4$ using a preliminary version of the MEGAFLOW galaxy catalog. With the full DR2 catalogue in hand, we will revisit in a separate paper the Mg II covering fraction for galaxies across the full redshift range $0.3 < z < 1.5$, as a function of azimuthal angle, and galaxy properties. But, one should address the potential impact of the pre-selection of sight-lines (§ 2). Using the DR2 galaxy catalog in Cherrey et al. (2024), we investigated the covering fraction of Mg II in groups of more than 5 galaxies.

Such *galaxy-centered* analysis is in fact possible in MEGAFLOW for a number of reasons. First, each MUSE field has $\approx$ 50 galaxies at $0.3 < z < 1.5$ observed over 2000 independent channels taking into account the spectral resolution, thus the pre-selection of fields only affects 5-10% of the sample. Second, the shape of the REW distribution dn/dW in MEGAFLOW is consistent with that of field/random sight-lines as discussed in § 4.1, and Fig. 4 and as noted in Schroetter et al. (2021). One should note that if the pre-selection of sight-lines would bias the results, the galaxy covering fractions in Schroetter et al. (2021) do not seem to be different from other surveys such as (e.g. Nielsen et al. 2013b; Lan 2020; Huang et al. 2021; Dutta et al. 2020).

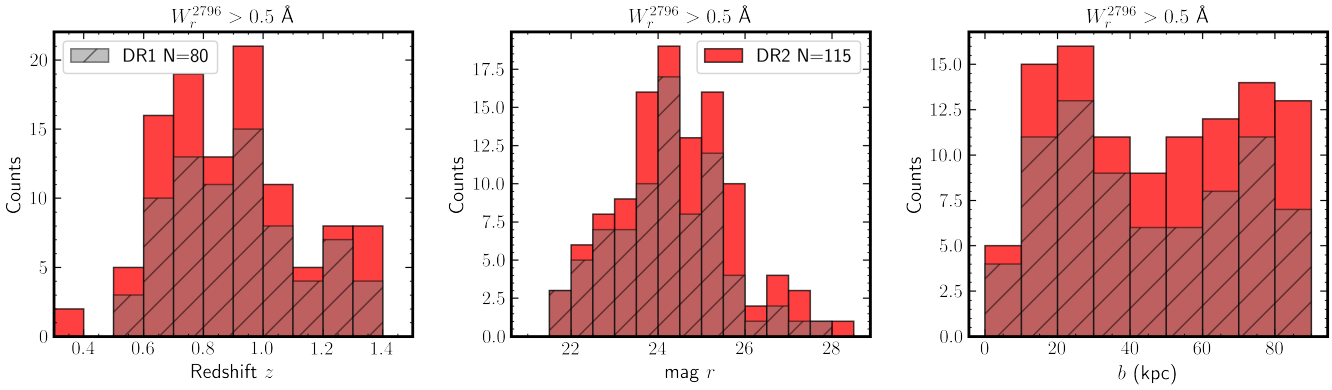

Fig. 11: Comparison between the DR2 and DR1 galaxy sample of galaxies within ±500 km s^{-1} around each Mg II absorption system and within 100 kpc. The left, middle and right panels show the redshift, magnitude and impact parameter distributions for galaxies in the redshift range $0.3 < z_{\rm abs} < 1.5$, respectively.

Nonetheless in order to further quantify the effect of our pre-selection, we perform the following experiment. We populated MUSE-like fields with galaxies, each with their own CGM (assumed to be a gas sphere). After applying a MEGAFLOW pre-selection, one can compute the covering fraction on these selected fields and compare it the covering fraction obtained using all fields (down to the same REW limit).

In particular, we generated 50 MUSE-like fields (500×500 pkpc in projected size corresponding to 1×1 arcmin), and drew 100 galaxies per field from a Poisson distribution across a redshift range ($0.4 < z < 1.4$) assigning a stellar mass from $\log M = 9.5$ to $\log M = 11.5$ according to a power law distribution of -1.5. We then assign a truncated sphere of gas around each galaxy (similar to Tinker & Chen 2008), with the gas density following a power law $\rho \propto r^{-\alpha}$ with $\alpha \approx 2 - 1.5$, truncated at $R_{\rm tr}$ =100 kpc. We set the normalization of the density profile such that the column density reaches $\sim 10^{20}$ cm^{-2} at 10 kpc adding a mass dependence ($\propto 0.3 \log M$) following the observed relation (Chen et al. 2010a). One can then compute the line-of-sight column density for each intercepted sphere and transform it into a REW using the $W_{\rm r}^{2796} - N_{\rm H\,I}$ relation from Ménard & Chelouche (2009). The resulting equivalent widht $W_{\rm r}^{2796}$ distribution is shown in Fig. 14 and is in good agreement with the observed distribution of strong absorbers (Nestor et al. 2005; Zhu & Ménard 2013).

For each field, we compute the number of absorptions with a $W_{\rm r}^{2796}$ greater than 0.6Å, corresponding to pre-selection of strong Mg II absorbers. Using only the ∼ 9-10 fields with 3 or more strong absorptions, mimicking the MEGAFLOW pre-selection, we computed the 2D covering fraction as a function of impact parameter and galaxy mass, $f_{\rm c}(\log b, \log M)$ using the method used in Schroetter et al. (2021) and Cherrey et al. (2024). Using only the selected sight-lines, the radius r_{50}, radius at which $f_{\rm c}(r_{50}|\log M = 10.5)$ is 50%, is

$$\log r_{50}|_{\log M=10.5} = 1.89 \pm 0.34. \quad (6)$$

When using all sight-lines, this radius is

$$\log r_{50}|_{\log M=10.5} = 1.91 \pm 0.21. \quad (7)$$

The mass dependence between $W_{\rm r}^{2796}$ and r_{50} is found to be $\propto (0.09 \pm 0.03) \log M$ for the selected sight-lines and $\propto (0.07 \pm 0.02) \log M$ for all sight-lines.

Apart from the larger statistical uncertainty due to the smaller number of fields, the values are very consistent with each other, and we conclude that there is no inherent bias in covering fractions due to the MEGAFLOW pre-selection criteria. See Cherrey et al. (2024) for similar arguments using different assumptions.

7. Discussion on [O II] vs continuum selected

The MEGAFLOW survey follows a *dual* galaxy identification process based on continuum and on emission lines (described in § 4.2) and thus allows for the identification of line emitters ([O II], Lyα) without any continuum in the MUSE observations. In the final catalog (DR2 v2.0) from the MUSE data, we find that 20% (30%) of galaxies with `ZCONF`≥ 2 (≥ 1) do not have a continuum ID (`WHITE_ID`), respectively. For [O II] emitters at $0.3 < z < 1.5$, the fraction is 8-15% depending on the redshift confidence `ZCONF` flag (see Table 8). For the low-redshift galaxies with `ZCONF`≥ 2 that are within 100 kpc and 500 km s^{-1} of a Mg II absorption, 13 out of 138 are detected only from their emission lines. For the *primary* galaxies within 100 kpc, 5 out of 58 are detected only from their emission lines. Hence, 10% of galaxies at $0.3 < z < 1.5$ are detected only from their emission lines.

However, not all sources without WHITE_ID are faint objects below the detection limit. Fig. 15 shows the SDSS r magnitude distribution of these galaxies without WHITE_ID. At high redshifts ($z > 2.8$), the top panel reveals that almost all have $r = 26$—28 mag, i.e. are below the completeness limit. At low redshifts ($z < 1.5$), the bottom panel reveals a population of galaxies without WHITE_ID but with bright $r < 26$ mag, which can often be traced to failed deblending, or to bright foreground/background object contaminating the flux measurement. The green histogram shows the 13 galaxies with `ZCONF`≥ 2 that are within 100 kpc and 500 km s^{-1} of Mg II absorptions, very relevant for the MEGAFLOW survey.

The advantage of the dual detection method can be seen in Figure 12(left), which shows the r-band magnitude versus the [O II] flux for the *primary* galaxies in MEGAFLOW

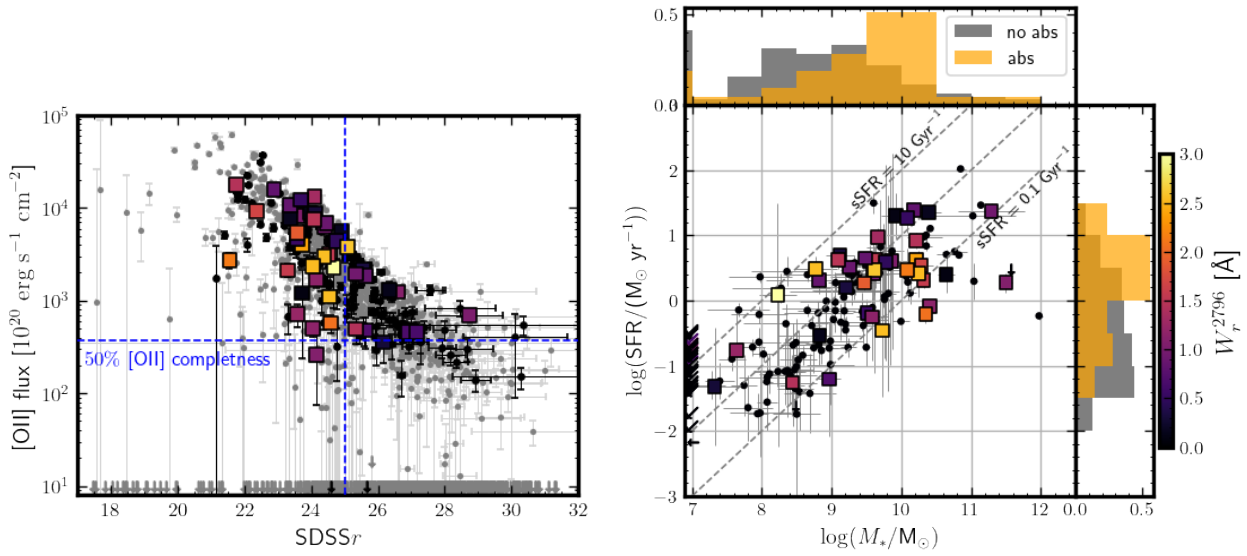

Fig. 12: *Left:* Measured [O II] flux versus SDSS r magnitude recomputed with PHOTUTILS. The full MEGAFLOW sample is represented with gray dots. Colored and black dots represent respectively *primary* galaxies associated and not associated with a counterpart absorption. Galaxies with no detected [O II] flux are represented by downward arrows. *Right:* Estimated stellar mass versus estimated SFR for the *primary* galaxies. The top and right histograms present respectively the stellar mass distribution and the SFR distribution for the galaxies associated (orange) and not associated (gray) with a Mg II absorption. Arrows on the left indicates galaxies without stellar mass estimation and/or no SFR estimation (because no [O II] emission detected). The primary galaxies associated with an absorption are colored according to the Mg II absorption rest-frame equivalent width. Error bars are 1σ uncertainties.

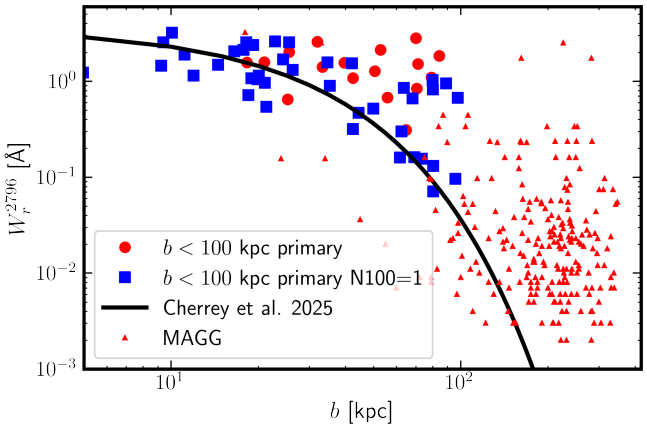

Fig. 13: REW (W_r^{2796}) vs impact parameter (b) for *primary* absorption-galaxy pairs within 100 kpc. The solid squares (circles) represent the pairs with only 1 galaxy (mulitple galaxies) within 100 kpc. Cherrey et al. (2025) investigates the W_r^{2796}-b relation of isolated galaxies and its dependence with the physical properties of the host. The triangles represent the MAGG sample (Dutta et al. 2020).

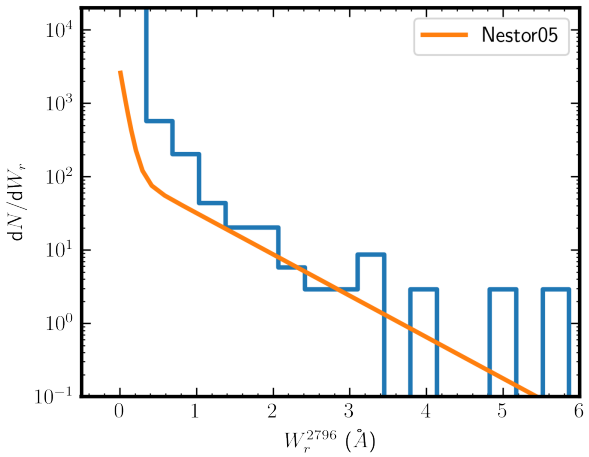

Fig. 14: Equivalent width distribution W_r^{2796} for mock galaxies in 50 MUSE-like fields. The solid line represents the observed distribution of strong Mg II absorbers from Nestor et al. (2005).

with or without Mg II absorption. From this figure, one sees that the FELINE line detection allows us to detect object beyond the continuum limit of $r \simeq 25$ mag. Figure 16 shows two examples of galaxies with [O II] emission and no continuum.

Similarly, in the Muse eXtremely Deep Field [MXDF; 140hr] of Bacon et al. (2023) who performed also a dual continuum and emission line detection, there are 175 out of 886 Lyα emitters (20%), which have no counterparts in the HST catalog (Rafelski et al. 2015) and 96 out 886 Lyα emitters (10%) have no detectable signal in the deep HST/UDF images. For comparison, the MAGG sample (Lofthouse et al. 2020) is based on continuum identification and does not include blind emission line galaxies. Similarly, the QSAGE sample (Bielby et al. 2019) is based on continuum identification on shallow 250s WFC3 F140W images. The sample from the MUSE Ultra Deep Field [MUDF; 150hr] of Fossati

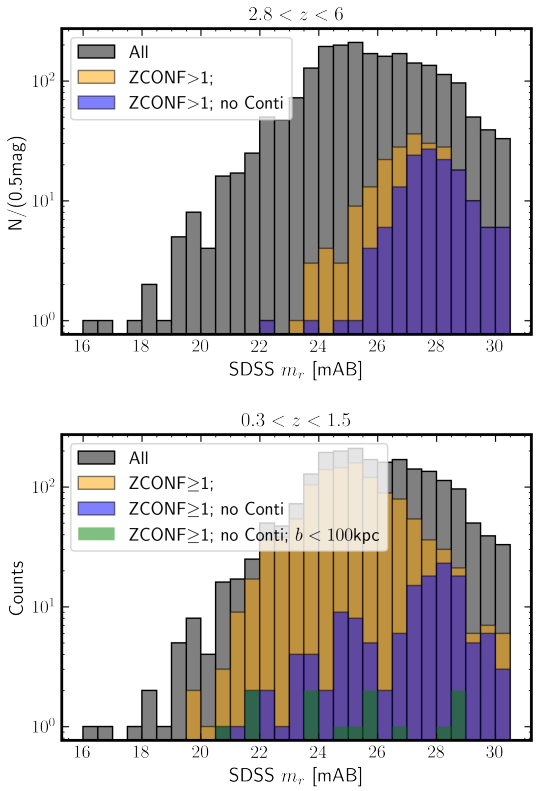

Fig. 15: Number counts for galaxies without continuum detection, without a `WHITE_ID`. The bottom (top) panel shows the distributions for low (high) redshift galaxies with $0.3 < z < 1.5$ ($2.8 < z < 6$) respectively. Both panels show that there is a significant popultion of galaxies detected solely on their emission line with `FELINE`.

Table 8: Galaxies without continuum or without FELINE detection.

ZCONF[a]	Redshift[b]	$N_{\rm tot}$[c]	no cont.[d]	no FEL[e]
1, 2, 3	All	1998	730	150
2, 3	All	1473	308	90
1, 2, 3	$0.35 < z < 1.5$	1151	170	73
2, 3	$0.35 < z < 1.5$	978	84	53

Notes. [(a)] Redshift confidence flag `ZCONF`. [(b)] Redshift range. [(c)] Number of sources. [(d)] Number of galaxies without continuum. [(e)] Number of galaxies without [O II].

et al. (2019) and Revalski et al. (2023) used deep (6.5hr) continuum F140W images for their catalog identification.

8. Conclusions

In this paper, we present the MEGAFLOW survey, a MUSE and UVES survey designed to better understand the CGM using low-ionization metal Mg II lines in 22 QSO fields. We describe the survey strategy (§ 2) and detail the MUSE and UVES data (§ 3) along with the data-products (4).

As discussed in § 2, the MEGAFLOW survey targeted 22 QSO fields with at least three Mg II absorptions lines with rest-frame $W_{\rm r}^{2796} \gtrsim 0.5$ Å, leading to 79 Mg II absorption lines. From the UVES spectra, we found additional Mg II absorption lines, leading to a total of 127 Mg II absorption lines. The rest-frame equivalent width distribution follows the expected power-law distribution of random sight-lines, albeit with a boosted normalization (Fig. 4)

Regarding this MUSE GTO program, the observations taken between 2014 and 2019, cover 22 arcmin^2, two fields (J0014−0028, J0937+0656) were observed at 10-11hr depths, while the other 20 fields were observed at 2-5hr depths. The 3σ sensitivity for emission lines at 7000Å is typically 5×10^{-19} erg s^{-1} cm^{-2} arcsec^{-2} for the 10hr depth cubes, and 7.5×10^{-19} erg s^{-1} cm^{-2} arcsec^{-2} for the 3-4hr depth cubes. As discussed in § 4.3, the 50% completeness limit for the 10hr (2.5hr) cubes is $3.7^{+0.8}_{-0.6} \times 10^{-18}$erg s^{-1} cm^{-2} ($7.07^{+1.6}_{-1.3} \times 10^{-18}$erg s^{-1} cm^{-2}) [O II] emitters at $\approx$ 7000 Å, and is approximately $i \sim m_{F775W} \approx$26 $m_{\rm AB}$ (25.2 $m_{\rm AB}$) for continuum sources, respectively.

The final catalog (v2.0) from the MEGAFLOW survey contains 2427 sources, which includes 22 Quasars, 57 stars, 2020 galaxies with `ZCONF`$\geq$ 1 and 350 sources with no redshifts (`ZCONF`= 0). As discussed in § 4.2, we use a dual galaxy identification process based both on continuum (using `SExtractor`; Bertin & Arnouts 1996) and on [O II] emission lines (using `FELINE`; Wendt et al. submitted), an approach similar to the MUSE UDF analysis of Bacon et al. (2023). This approach has the significant advantage that [O II] emitters without continuum counterpart can be identified (Fig. 16). Overall, we find a third (718/1998) of galaxies with redshift flag `ZCONF`$\geq$ 1 have no continuum detection down to $r \approx 28.5$ $m_{\rm AB}$. For [O II] emitters at $0.3 < z < 1.5$, we find 8 (15) per cent of galaxies without a continuum detection for sources with ZCONF ≥ 2 (≥ 1) (Table 8).

For strong ($W_{\rm r}^{2796} \gtrsim 0.5$ Å) Mg II absorbers in the redshift range $0.35 < z < 1.5$, where [O II] can be identified in the MUSE wavelength coverage, the success rate of detecting the host galaxy within 100 kpc is 90% (Table 7). The mean number of galaxies per absorber is ~ 3 within the MUSE FOV, and 40 (20) absorbers have 1 (2) galaxies within 100 kpc.

All but two of the host galaxies have SFR greater than 1 $M_\odot$ yr^{-1} and stellar masses above 10^9 $M_\odot$, after performing SED fitting on the MUSE data using 13 pseudo-medium filters. Given that this MUSE survey is sensitive to galaxies with $M_\star \gtrsim 10^{7.5}$ and SFR $\gtrsim 0.01$ $M_\odot$ yr^{-1} (Fig. 12), we can rule out the role of LMC-like satellites for strong Mg II systems with $W_{\rm r}^{2796} > 0.5$ Å, as we would have detected satellites with mass ratio 1 : 20 or greater.

Acknowledgements. This study is based on observations collected at the European Southern Observatory under ESO programs listed in Table 2 and 3. This work has been carried out thanks to the support of the ANR FOGHAR (ANR-13-BS05-0010), the ANR 3DGasFlows (ANR-17-CE31-0017), and the OCEVU Labex (ANR-11-LABX-0060). LW acknowledges funding by the European Research Council through ERC-AdG SPECMAP-CGM, GA 101020943. RB acknowledges support from the ANR L-INTENSE (ANR-CE92-0015).

Software: This work made use of the following open source software: GalPaK^{3D} (Bouché et al. 2015), FELINE (Wendt et al. submitted), ZAP (Soto et al. 2016), MPDAF (Piqueras et al. 2019), Matplotlib (Hunter 2007), NumPy (Van Der Walt et al. 2011), Astropy (The Astropy Collaboration et al. 2018), MAOPPY (Fétick et al. 2019), Pampelmuse (Kamann et al. 2013), Photu-

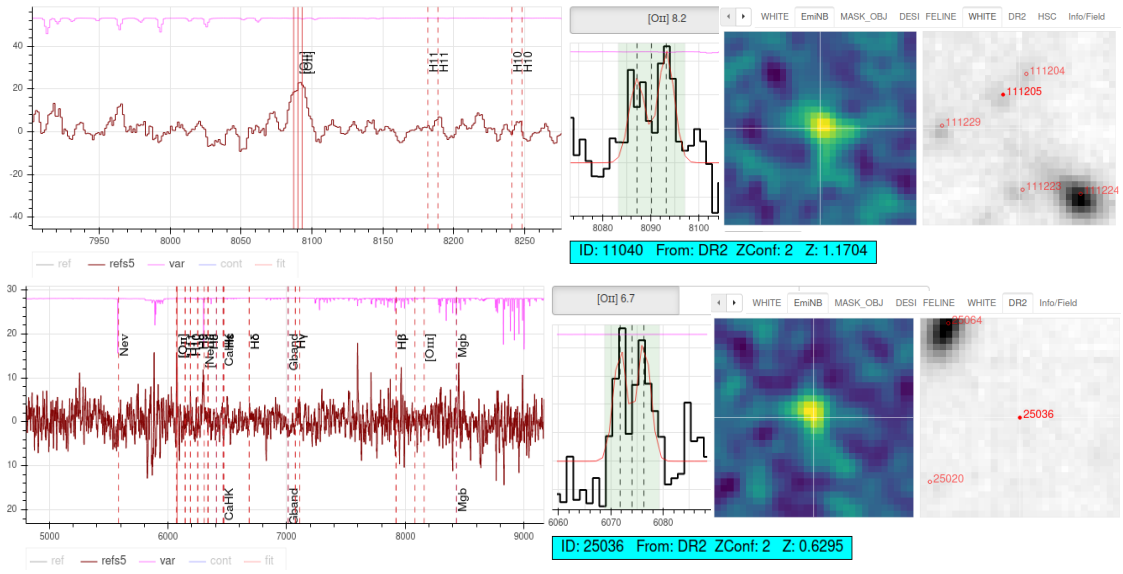

Fig. 16: Examples of [O II] emitters without continuum for source ID= 11040 and ID= 25036. More information available on the AMUSED interface. For each source, the MUSE spectra, the [O II] emission, the pseudo narrow-band image at [O II], and the white-light continuum image are shown.

TILS (Bradley et al. 2022), DUSTMAPS (Green 2018), and PYMC3 (Salvatier et al. 2016).

Data availability

The MUSE and UVES raw data used for this article are available in the ESO archive [13]. The reduced MUSE datacubes are available on the MuseWise website [14] The MUSE and UVES products, the MEGAFLOW catalogs and MUSE advanced data products are also available on the AMUSED website [15].

References

Abbas A., Churchill C. W., Kacprzak G. G., Lidman C., Guatelli S., Bellstedt S., 2024, ApJ, 966, 242
Amorisco N. C., Bertin G., 2010, A&A, 519, A47
Bacon R., et al., 2010, in Society of Photo-Optical Instrumentation Engineers (SPIE) Conference Series. p. 8, doi:10.1117/12.856027
Bacon R., et al., 2017, A&A, 608, A1
Bacon R., et al., 2021, A&A, 647, A107
Bacon R., et al., 2023, A&A, 670, A4
Bahcall J. N., Spitzer Lyman J., 1969, ApJ, 156, L63
Bergeron J., Boissé P., 1991, A&A, 243, 344
Bergeron J., Cristiani S., Shaver P. A., 1992, A&A, 257, 417
Bergeron J., et al., 1994, ApJ, 436, 33
Bertin E., Arnouts S., 1996, A&AS, 117, 393
Bielby R., Crighton N. H. M., Fumagalli M., Morris S. L., Stott J. P., Tejos N., Cantalupo S., 2017, MNRAS, 468, 1373
Bielby R. M., et al., 2019, MNRAS, 486, 21
Bouché N. F., McConway K., 2019, Bioelectromagnetics, 40, 539
Bouché N. F., Murphy M. T., Péroux C., Csabai I., Wild V., 2006, MNRAS, 371, 495
Bouché N. F., Murphy M. T., Péroux C., Davies R., Eisenhauer F., Förster Schreiber N. M., Tacconi L., 2007, ApJ, 669, L5
Bouché N. F., Carfantan H., Schroetter I., Michel-Dansac L., Contini T., 2015, AJ, 150, 92

[13] http://archive.eso.org.
[14] https://http://muse-dbview.hpc.rug.nl/QaView.
[15] https://amused.univ-lyon1.fr/project/megaflow.

Bradley L., et al., 2022, astropy/photutils: 1.5.0, doi:10.5281/zenodo.6825092, https://doi.org/10.5281/zenodo.6825092
Brinchmann J., Charlot S., White S. D. M., Tremonti C., Kauffmann G., Heckman T., Brinkmann J., 2004, MNRAS, 351, 1151
Bruzual G., Charlot S., 2003, MNRAS, 344, 1000
Calzetti D., Armus L., Bohlin R. C., Kinney A. L., Koornneef J., Storchi-Bergmann T., 2000, ApJ, 533, 682
Cardelli J. A., Clayton G. C., Mathis J. S., 1989, ApJ, 345, 245
Chabrier G., 2003, PASP, 115, 763
Chen H.-W., Tinker J. L., 2008, ApJ, 687, 745
Chen H.-W., Helsby J. E., Gauthier J.-R., Shectman S. A., Thompson I. B., Tinker J. L., 2010a, ApJ, 714, 1521
Chen H., Wild V., Tinker J. L., Gauthier J., Helsby J. E., Shectman S. A., Thompson I. B., 2010b, ApJ, 724, L176
Chen H.-W., et al., 2020, MNRAS, 497, 498
Cherrey M., et al., 2025, A&A (accpeted)
Cherrey M., et al., 2024, MNRAS, 528, 481
Churchill C. W., Trujillo-Gomez S., Nielsen N. M., Kacprzak G. G., 2013, ApJ, 779, 87
DeFelippis D., Bouché N. F., Genel S., Bryan G. L., Nelson D., Marinacci F., Hernquist L., 2021, ApJ, 923, 56
Dekker H., D'Odorico S., Kaufer A., Delabre B., Kotzlowski H., 2000, in Iye M., Moorwood A. F., eds, Proc. SPIEVol. 4008, Optical and IR Telescope Instrumentation and Detectors. pp 534–545, doi:10.1117/12.395512
Dutta R., et al., 2020, MNRAS, 499, 5022
Eisenhauer F., et al. 2003, in Iye M., Moorwood A. F. M., eds, Instrument Design and Performance for Optical/Infrared Ground-based Telescopes. Edited by Iye, Masanori; Moorwood, Alan F. M. Proceedings of the SPIE, Volume 4841, pp. 1548-1561 (2003).. pp 1548–1561
Fétick R. J. L., et al., 2019, A&A, 628, A99
Fossati M., et al., 2019, MNRAS, 490, 1451
Freundlich J., Bouché N. F., Contini T., Daddi E., Zabl J., Schroetter I., Boogaard L., Richard J., 2021, MNRAS, 501, 1900
Fumagalli M., Prochaska J. X., Kasen D., Dekel A., Ceverino D., Primack J. R., 2011, MNRAS, 418, 1796
Gauthier J.-R., 2013, MNRAS, 432, 1444
Gauthier J., Chen H., Tinker J. L., 2009, ApJ, 702, 50
Gilbank D. G., Baldry I. K., Balogh M. L., Glazebrook K., Bower R. G., 2010, MNRAS, 405, 2594
Gilbank D. G., Baldry I. K., Balogh M. L., Glazebrook K., Bower R. G., 2011, MNRAS, 412, 2111
Green G., 2018, The Journal of Open Source Software, 3, 695
Herenz E. C., Wisotzki L., 2017, A&A, 602, A111

Hinton S. R., Davis T. M., Lidman C., Glazebrook K., Lewis G. F., 2016, Astronomy and Computing, 15, 61
Ho S. H., Martin C. L., Turner M. L., 2019, ApJ, 875, 54
Ho S. H., Martin C. L., Schaye J., 2020, ApJ, 904, 76
Hoffman M. D., Gelman A., 2014, Journal of Machine Learning Research, 15, 1593
Huang Y.-H., Chen H.-W., Shectman S. A., Johnson S. D., Zahedy F. S., Helsby J. E., Gauthier J.-R., Thompson I. B., 2021, MNRAS, 502.4743
Hunter J. D., 2007, Computing in Science and Engineering, 9, 90
Kacprzak G. G., Murphy M. T., Churchill C. W., 2010, MNRAS, 406, 445
Kacprzak G. G., Churchill C. W., Barton E. J., Cooke J., 2011, ApJ, 733, 105
Kamann S., Wisotzki L., Roth M. M., 2013, A&A, 549, A71
Kimm T., Slyz A., Devriendt J., Pichon C., 2011, MNRAS, 413, L51
Koushan S., et al., 2021, MNRAS, 503, 2033
Lan T.-W., 2020, ApJ, 897, 97
Langan I., et al., 2023, MNRAS, 521, 546
Lanzetta K. M., Bowen D., 1990, ApJ, 357, 321
Lofthouse E. K., et al., 2020, MNRAS, 491, 2057
Lundgren B. F., et al., 2009, ApJ, 698, 819
Lundgren B. F., et al., 2021, ApJ, 913, 50
Mary D., Bacon R., Conseil S., Piqueras L., Schutz A., 2020, A&A, 635, A194
Ménard B., Chelouche D., 2009, MNRAS, 393, 808
Mishra S., Muzahid S., 2022, ApJ, 933, 229
Murphy M., 2018, MTMurphy77/UVES_popler: UVES_popler: POst-PipeLine Echelle Reduction software, doi:10.5281/zenodo.1297190, `https://doi.org/10.5281/zenodo.1297190`
Murphy M. T., Kacprzak G. G., Savorgnan G. A. D., Carswell R. F., 2019, MNRAS, 482, 3458
Muzahid S., et al., 2020, MNRAS, 496, 1013
Navarro J. F., Frenk C. S., White S. D. M., 1997, ApJ, 490, 493
Nestor D. B., Turnshek D. A., Rao S. M., 2005, ApJ, 628, 637
Nestor D. B., Johnson B. D., Wild V., Ménard B., Turnshek D. A., Rao S., Pettini M., 2011, MNRAS, 412, 1559
Nielsen N. M., Churchill C. W., Kacprzak G. G., Murphy M. T., 2013a, ApJ, 776, 114
Nielsen N. M., Churchill C. W., Kacprzak G. G., 2013b, ApJ, 776, 115
Ono Y., et al., 2012, ApJ, 744, 83
Péroux C., Howk J. C., 2020, ARA&A, 58, 363
Péroux C., et al., 2019, MNRAS, 485, 1595
Pichon C., Pogosyan D., Kimm T., Slyz A., Devriendt J., Dubois Y., 2011, MNRAS, 418, 2493
Piqueras L., Conseil S., Shepherd M., Bacon R., Leclercq F., Richard J., 2019, in Molinaro M., Shortridge K., Pasian F., eds, Astronomical Society of the Pacific Conference Series Vol. 521, Astronomical Data Analysis Software and Systems XXVI. p. 545
Planck Collaboration et al., 2014, A&A, 571, A11
Planck Collaboration et al., 2016, A&A, 594, A13
Rafelski M., et al., 2015, AJ, 150, 31
Revalski M., et al., 2023, ApJS, 265, 40
Salvatier J., Wiecki T. V., Fonnesbeck C., 2016, PeerJ Comput. Sci., 2, e55
Schaerer D., de Barros S., 2009, A&A, 502, 423
Schroetter I., et al., 2016, ApJ, 833, 39
Schroetter I., et al., 2019, MNRAS, 490, 4368
Schroetter I., et al., 2021, MNRAS, 506, 1355
Schroetter I., Bouché N. F., Zabl J., Wendt M., Cherrey M., Langan I., Schaye J., Contini T., 2024, A&A, 687, 39
Shen S., Madau P., Guedes J., Mayer L., Prochaska J. X., Wadsley J., 2013, ApJ, 765, 89
Soto K. T., Lilly S. J., Bacon R., Richard J., Conseil S., 2016, MNRAS,
Spitzer Lyman J., 1956, ApJ, 124, 20
Steidel C. C., 1993, in Shull J. M., Thronson H. A., eds, The Environment and Evolution of Galaxies. Kluwer, Dordrecht, p. 263
Steidel C. C., 1995, in Meylan G., ed., QSO Absorption Lines. ESO Astrophysics Symposia. Springer-Verlag, Berlin, Germany, p. 139
Steidel C. C., Dickinson M., Persson S. E., 1994, ApJ, 437, L75
Steidel C. C., Bowen D. V., Blades J. C., Dickinson M., 1995, ApJ, 440, L45
Steidel C. C., Dickinson M., Meyer D. M., Adelberger K. L., Sembach K. R., 1997, ApJ, 480, 568
Steidel C. C., Kollmeier J. A., Shapley A. E., Churchill C. W., Dickinson M., Pettini M., 2002, ApJ, 570, 526
The Astropy Collaboration et al., 2018, preprint, (`arXiv:1801.02634`)
Tinker J. L., Chen H.-W., 2008, ApJ, 679, 1218
Tumlinson J., Peeples M. S., Werk J. K., 2017, ARA&A, 55, 389
Valentijn E. A., et al., 2017, in Brescia M., Djorgovski S. G., Feigelson E. D., Longo G., Cavuoti S., eds, Vol. 325, Astroinformatics. pp 333–340 (`arXiv:1612.05996`), doi:10.1017/S1743921317000254
Van Der Walt S., Colbert S. C., Varoquaux G., 2011, Computing in Science and Engineering, 13, 22
Weilbacher P. M., Streicher O., Urrutia T., Pécontal-Rousset A., Jarno A., Bacon R., 2014, in Manset N., Forshay P., eds, Astronomical Society of the Pacific Conference Series Vol. 485, Astronomical Data Analysis Software and Systems XXIII. p. 451 (`arXiv:1507.00034`)
Weilbacher P. M., et al., 2020, A&A, 641, A28
Wendt M., Bouché N. F., Zabl J., Schroetter I., Muzahid S., 2021, MNRAS, 502, 3733
Wendt M., Henschel M., Soth O. F., submitted, JOSS
Weng S., Péroux C., Ramesh R., Nelson D., Sadler E. M., Zwaan M., Bollo V., Casavecchia B., 2024, MNRAS, 527, 3494
York D. G., et al., 2000, AJ, 120, 1579
Zabl J., Freudling W., Møller P., Milvang-Jensen B., Nilsson K. K., Fynbo J. P. U., Le Fèvre O., Tasca L. A. M., 2016, A&A, 590, A66
Zabl J., et al., 2019, MNRAS, 485, 1961
Zabl J., et al., 2020, MNRAS, 492, 4576
Zabl J., et al., 2021, MNRAS, 507, 4294
Zhu G., Ménard B., 2013, ApJ, 770, 130

[1] Univ. Lyon1, Ens de Lyon, CNRS, Centre de Recherche Astrophysique de Lyon (CRAL) UMR5574, F-69230 Saint-Genis-Laval, France
e-mail: `nicolas.bouche@univ-lyon1.fr` [16]
[2] Institut für Physik und Astronomie, Universität Potsdam, Karl-Liebknecht-Str. 24/25, 14476 Potsdam, Germany
[3] Institute for Computational Astrophysics and Department of Astronomy & Physics, Saint Mary's University, 923 Robie Street Halifax, Nova Scotia B3H 3C3, Canada
[4] Institut de Recherche en Astrophysique et Planétologie (IRAP), Université de Toulouse, CNRS, UPS, F-31400 Toulouse, France
[5] European Southern Observatory (ESO), Karl-Schwarzschild-Str. 2, 85748 Garching b. München, Germany
[6] Inter-University Centre for Astronomy & Astrophysics (IUCAA), Post Bag 04, Pune, India, 411007
[7] Leiden Observatory, Leiden University, PO Box 9513, NL-2300 RA Leiden, the Netherlands
[8] Aix Marseille Univ., CNRS, CNES, LAM, Marseille, France
[9] Canada-France-Hawaii Telescope, 65-1238 Mamalahoa Highway, Kamuela, HI 96743, USA
[10] Leibniz-Institut für Astrophysik Potsdam (AIP), An der Sternwarte 16, 14482 Potsdam, Germany

Appendix A: UVES EW limits

Fig. A.1 shows the rest-frame $W_{\rm r}^{2796}$ limits (3σ) for each field used in Fig. 3 as a function of redshifts which ranges from 0.05 to 0.1Å.

Appendix B: Description of the catalogs and products

Table B.1 describes the content of the galaxy catalog. Table B.2 describes the content of the Mg II absorption catalog. Table B.3 describes the available MUSE datasets and associated files.

Fig. B.1 shows an example of an html file displaying the summary information of each sources, available on the `AMUSED` interface.

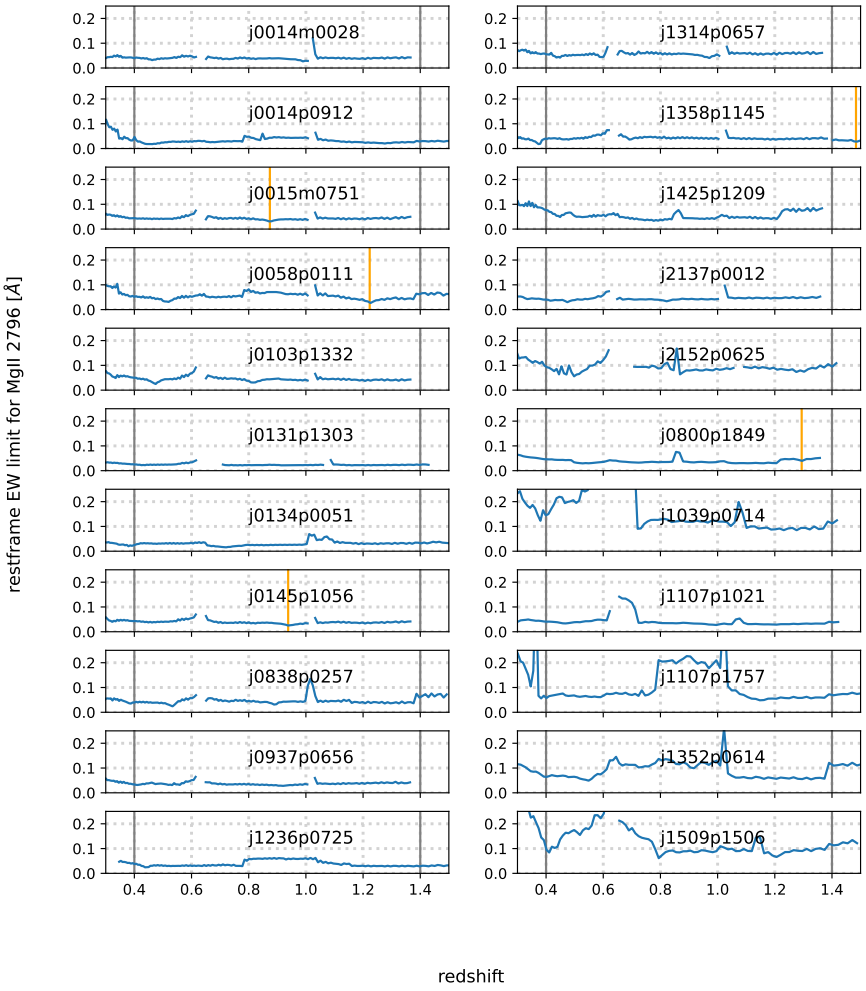

Fig. A.1: Rest-frame $W_{\rm r}^{2796}$ limits (3-σ) for Mg II 2796 per field and redshift. The *grey bars* indicate the redshift range of the survey and the *orange bars* indicate the QSO's redshift if below z=1.5.

Table B.1: Column description of the main galaxy catalog.

Col.name	Description
ID	Unique source identifier
FIELD_NAME	Short name of the field
DATASET	MUSE Dataset (`beta`, `psfsub`)
FROM	Source origin (FELINE, MANUAL, WHITE)
Z	Redshift
Z_ERR	Redshift error
ZCONF	Redshift Confidence (0,1,2,3)
is_QSO	Boolean flag for quasars
is_star	Boolean flag for stars
is_blended	Boolean flag for source blending
RA	Right ascension (deg)
DEC	Declination (deg)
B_KPC	Impact parameter in kpc
B_ARCSEC	Impact parameter in arcsec
REFSPEC	Type of spectrum extraction
REFCENTER	Reference center
FELINE_ID	Source identifier from `FELINE` (§ 4.2.2)
WHITE_ID	Source identifier from `WHITE` (§ 4.2.3)
MANUAL_ID	Source identifier from manual entry
SDSS_r	r-magnitude
SDSS_r _ERR	r-magnitude error
SDSS_i	i-magnitude
SDSS_i _ERR	i-magnitude error
MAG_F775W	F775W magnitude
MAG_F775W_ERR	F775W magnitude error
in_DR1	Boolean flag for DR1 sources
DR1_id	ID in DR1

Table B.2: Column description of the Mg II absorption catalog

Col.name	Description
asb_id	absorption ID
FIELD_NAME	Short name of the field
z_abs	Absorption redshift
REW_2796	$W_{\rm r}^{2796}$(Å)
sig_REW_2796	$W_{\rm r}^{2796}$uncertainty (1σ)

Table B.3: List of MUSE datasets and associated files

Field name	Filename	Dataset	Description
J1122p3344	`J1122p3344_dr2_zap.expmap_2d_wcs.fits`		2D Exposure map
J1122p3344	`J1122p3344_dr2_zap_wpsf2.corrEBV.fits`	beta	3D Data cube[a]
J1122p3344	`J1122p3344_dr2_zap_wpsf2_qsosub.corrEBV.fits`	psfsub	3D Data cube[a]
J1122p3344	`J1122p3344_dr2.corrspec.fits`		1D Applied E(B-V) correction

Notes. [(a)] Filename. The datacubes are in units of 10^{-20} erg s^{-1} cm^{-2} Å^{-1}.

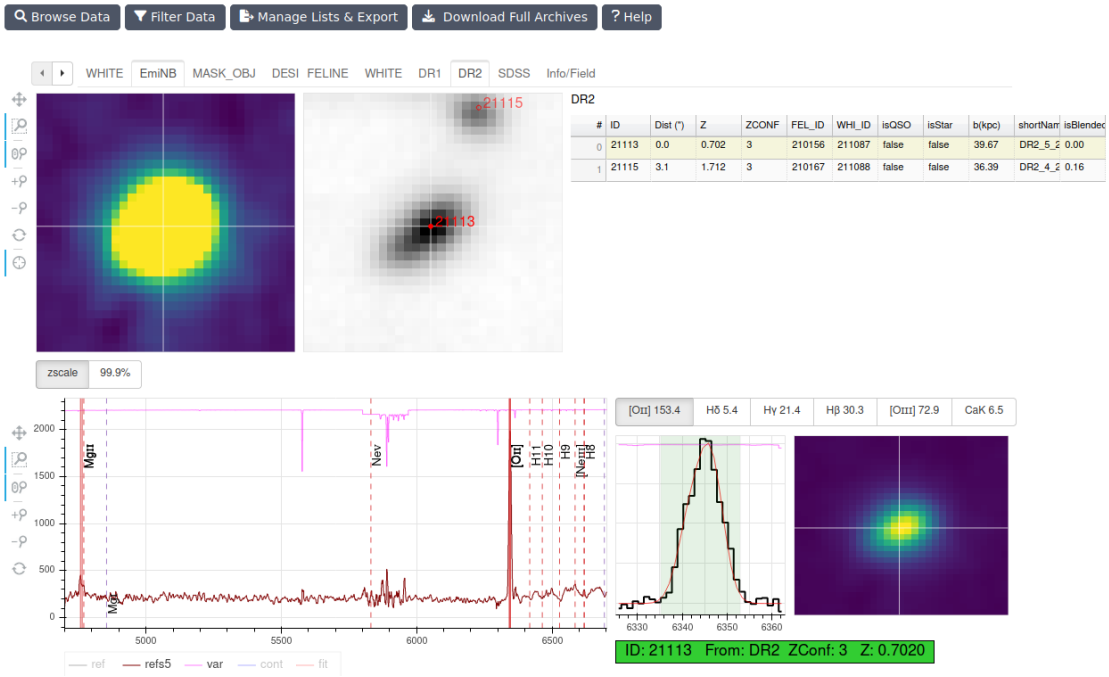

Fig. B.1: Example of a html file summarizing the information regarding each source available from the AMUSED web interface. This source is the $z = 0.702$ galaxy ID 21113 with a Mg II halo presented in Zabl et al. (2021).